

Review

# Advanced Trends in Metallurgy and Weldability of High-Strength Cold-Resistant and Cryogenic Steels

Andrei I. Rudskoi and Sergey G. Parshin \* 

Institute of Mechanical Engineering, Materials and Transport, Peter the Great St. Petersburg Polytechnic University, Polytechnicheskaya, 29, 195251 St. Petersburg, Russia; a.rudskoy@spbstu.ru

\* Correspondence: parshin@spbstu.ru; Tel.: +7-812-552-6355

**Abstract:** Thermomechanical Controlled Processing (TMCP), the initial microstructure and mechanical properties of rolled products made of high-strength steels, have a significant influence on the properties and reliability of welded structures for low temperature and cryogenic service. This paper systematizes advanced research trends in the field of metallurgy and weldability of high-strength cold-resistant and cryogenic steels. The classification and properties of high-strength steels are given and TMCP diagrams and phase transformations are considered. Modern methods of improving the viscoplasticity of rolled steel and welded joints are analyzed. The problems of the weldability of high-strength steels are reduction of impact toughness at low temperatures, hydrogen embrittlement, anisotropy, and softening of welded joints in the heat-affected zone. The authors propose a systemic concept and methods for improving the metallurgy and weldability of high-strength steels for low temperature and cryogenic service.

**Keywords:** metallurgy; high-strength cold-resistant and cryogenic steels; thermomechanical controlled processing; weldability



**Citation:** Rudskoi, A.I.; Parshin, S.G. Advanced Trends in Metallurgy and Weldability of High-Strength Cold-Resistant and Cryogenic Steels. *Metals* **2021**, *11*, 1891. <https://doi.org/10.3390/met11121891>

Academic Editors: Namhyun Kang and Frank Czerwinski

Received: 19 October 2021  
Accepted: 20 November 2021  
Published: 23 November 2021

**Publisher's Note:** MDPI stays neutral with regard to jurisdictional claims in published maps and institutional affiliations.



**Copyright:** © 2021 by the authors. Licensee MDPI, Basel, Switzerland. This article is an open access article distributed under the terms and conditions of the Creative Commons Attribution (CC BY) license (<https://creativecommons.org/licenses/by/4.0/>).

## 1. Introduction

High-strength cold-resistant and cryogenic steels are widely used for icebreakers, gas carriers, hydrogen storage, hydrocarbon production and transportation, wind turbines, offshore platforms, railroads, and the automotive industry. The history of traditional high-strength steel (HSS) metallurgy began with the creation of low-alloy Si-Mn ferritic-pearlitic steels with a carbon content of <0.2% [1–3]. The micro-alloying of V, Nb, Ti, and Thermomechanical Controlled Processing (TMCP) allowed the achievement of a fine-grained microstructure, increasing strength and impact toughness with a decrease in carbon content < 0.15% [1–3].

Subsequent development of TMCP and the application of accelerated cooling with tempering allowed for obtaining ferritic–bainitic and ferritic–martensitic microstructures of steels with reduced carbon content <0.1%. This microstructure has a fine-dispersed morphology with distributed and dispersed carbides and carbonitrides, and has a high impact toughness. Micro-alloying, optimization of TMCP, microstructure refinement, dispersion hardening, refining, and reduction of the anisotropy of rolled steel are used to improve plasticity and impact toughness of high-strength steels. Modern HSS have bainitic, bainitic–martensitic, martensitic–bainitic, and martensitic microstructures with low carbon content up to 0.05–0.02%. The production and development of high-strength steels are closely related to welding metallurgy and weldability, as arc and laser welding are used to make structures.

Research on the metallurgy and weldability of high-strength steels is actively developing all over the world. The main trends are increasing strength and impact toughness of steels, improving quality, and reducing the cost of alloying in steelmaking [4–7]. Among traditional and advanced high-strength steels for low-temperature and cryogenic service, about 15 groups of low- and high-alloy steels should be distinguished, as shown in Figure 1.

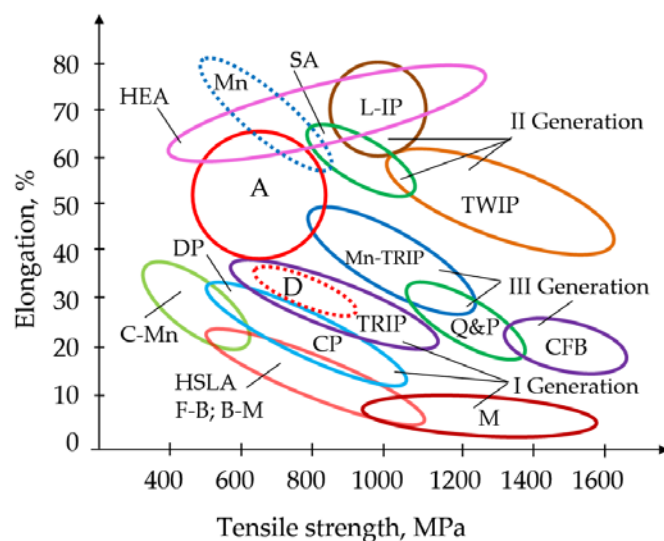


**Figure 1.** Mechanical properties of HSS and AHSS (Advanced High-Strength Steels) high-strength cold-resistant and cryogenic steels.

Figure 1 contains the following designations: C-Mn—pearlitic steels; HSLA—high-strength low-alloy steels; F-B—ferritic–bainitic steels; B-M—bainitic–martensitic steels; DP (Dual-Phase)—two-phase steels; CP—complex phase steels; D—duplex steels; TRIP (Transformation-Induced Plasticity)—metastable steels with induced plasticity; M—martensitic steels; TWIP (Twinning-Induced Plasticity)—austenitic high-manganese steels with induced plasticity; Mn-TRIP—medium-manganese TRIP steels; Q&P (Quenching and Partitioning)—martensitic–austenitic steels; CFB—carbide-free bainitic steels; A—austenitic steels; SA—superaustenitic steels; L-IP—lightweight steels with induced plasticity; Mn—high-manganese austenitic steels; HEA—high-entropy alloys.

Advanced steels have high strength, corrosion resistance, and high viscoplasticity at low temperatures, and can be considered as alternatives to Ni-, Ti-, Al-, and Cu-alloys for low temperature and cryogenic service, including hydrogen storage systems, as shown in Figure 2.

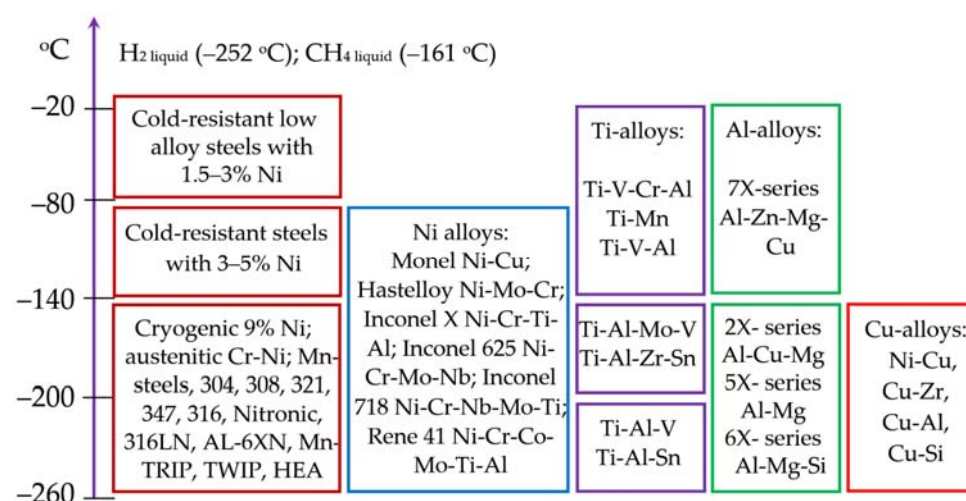


**Figure 2.** Steels and alloys for low-temperature and cryogenic service.

The scientific novelty of this paper consists in the analysis of problems of weldability and the systemic concept formulation of a relationship between the steelmaking, weldability and manufacturing of welded structures for low temperature and cryogenic service. The weldability of high-strength steels is linked to steelmaking, thermomechanical processing,

and the microstructural design of steels, based on a three-level system of processes, as shown in Figure 3.

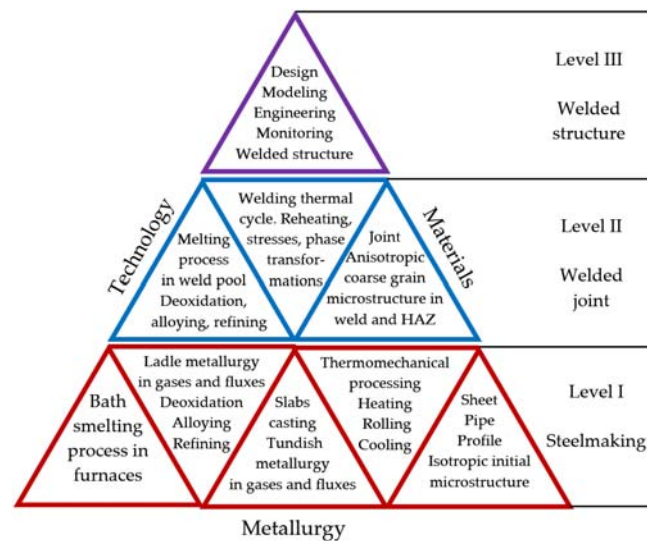


**Figure 3.** Multi-level system of processes for the manufacturing of welded structures.

The high quality of the manufacturing of welded structures is based on the quality in levels: steelmaking, welded joint, and welded structure. The most serious problem is the anisotropy and microstructure chemical-heterogeneity due to welding thermal cycle on level II. The anisotropy degree of the weld microstructure depends on the susceptibility of the initial microstructure of the rolled steels to the welding thermal cycle.

In our opinion, advanced current trends, and methods in the field of metallurgy and weldability for improving the mechanical properties, microstructure, and viscoplasticity of high-strength steels and welded joints can present as system, as shown in Figure 4.

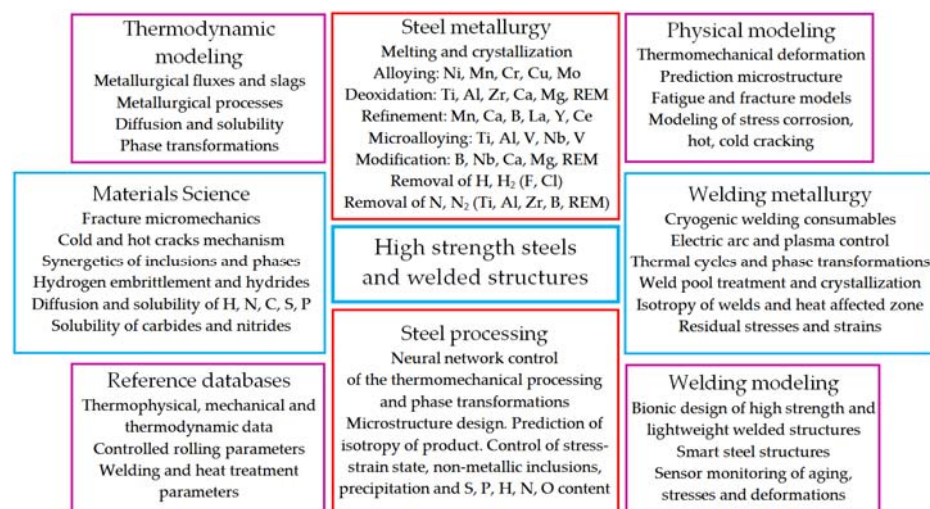


**Figure 4.** System of advanced trends and methods in the metallurgy and weldability of high-strength steels for welded structures for low temperature and cryogenic service.

The system of advanced trends and methods is based on the metallurgical relationship between the steelmaking and the manufacturing of welded structures.

The purpose of this work is to analyze and systematize the advanced trends and methods in the field of metallurgy and weldability of high-strength cold-resistant and cryogenic steels to achieve the high quality of welded structures.

## 2. Properties of High-Strength Steels

### 2.1. High-Strength Low-Alloy Steels

High-strength low-alloy steels (HSLA-steels) have the chemical composition, %: 0.04–0.25 C; 1–2 Mn; 0.4–3.5 Ni; <0.5 alloying elements Si, N, Cr, Mo, Ca, Al, REM, Zr. The formation of intermetallics, carbides, and carbonitrides through the alloying of Cu, Ti, V, and Nb is used for the dispersion hardening of the ferrite matrix. Reducing the grain size increases impact toughness while maintaining a high yield strength of over 460 MPa. The main method of production of these steels is TMCP [1].

High-strength steels are divided into six categories [8,9]: weather-resistant with phosphorus and copper alloying; micro-alloyed ferritic–pearlitic steels with less than 0.1% of the carbides and carbonitrides Nb, Ti, and V for dispersion hardening, grain refinement, and transformation temperature changes; low-alloy steels of controlled rolling from pearlitic C-Mn steels; low-carbon low-alloy bainite steels with acicular ferrite [10]; two-phase martensitic–ferritic steels with high impact toughness; steels with controlled form of nonmetallic inclusions with the alloying of Ca, REM, Zr, and Ti.

Hwang et al. [11] proposed the TMCP diagram of HSLA steel, %: 0.07 C; 0.25 Si; 1.9 Mn; 0.5 Ni; 0.6 Cr; 0.25 Mo; 0.06 Nb; 0.03 V; 0.015 Ti to achieve a strength of 980–1050 MPa and  $KV_{-70}$  of 50 J. According to the TMCP diagram, the process consists of heating to 1150 °C, slow cooling to 600 °C, and accelerated cooling from 600 °C during thermomechanical rolling in the recrystallization region and non-recrystallization region, as shown in Figure 5a.

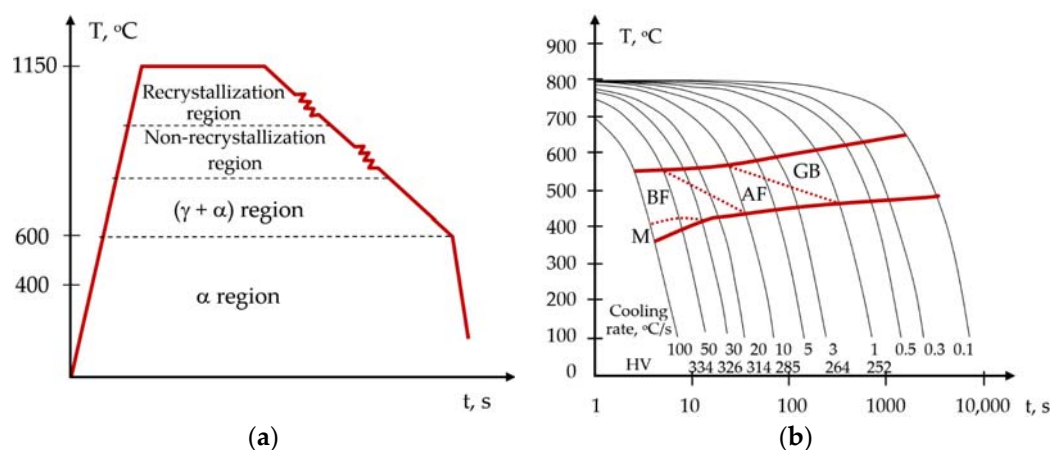


Figure 5. (a) TMCP diagram of HSLA steel Data from [11]. (b) CCT diagram of HSLA steel. Data from [9].

Cochrane [9] presented the CCT diagram for typical boron-containing HSLA steel, %: 0.05 C; 0.25 Si; 1.92 Mn; 0.067 Nb + Ti; 1.1 (Mo + Cr + Ni) and proved that the microstructure of the steel includes bainitic ferrite (BF), acicular ferrite (AF), grain boundary ferrite (GB), and martensite (M) at a cooling rate of 1–100 °C/s with a hardness of 252–334 HV, as shown in Figure 5b.

According to GOST R 52927-2015, used for shipbuilding and offshore structures in arctic conditions (rolled normal, increased- and high-strength steel for shipbuilding. Specifications in Russian), HSLA-steels for shipbuilding E, F, D 420–500 with index Arc (Arctic) have a strength of 530–770 MPa with impact energy  $KV_{-60}$  of minimum 80 J. Thermomechanical processing with accelerated cooling, hardening, and tempering are used for the production of cold-resistant steels. The steels have chemical composition, %: 0.008–0.12 C; 0.45–1.6 Mn; 0.1–0.4 Si; <1.3 Cr; <0.65 Cu; 0.55–2.15 Ni; <0.18 Mo; <0.005 S; <0.1 P, and micro-alloying elements: Al, Ti, V, and Nb, as shown in Table 1.

**Table 1.** Chemical composition of steels according to GOST R 52927-2015, wt%.

Steel	C	Mn	Si	Cr	Cu	Ni	Mo
D,E,F420W F420W <sup>Arc</sup> D,E,F460W F460W <sup>Arc</sup>	0.08–0.11	1.15–1.6	0.1–0.4	<0.2	0.3–0.6	0.65–1.05	<0.08
D,E,F500WF 500W <sup>Arc</sup>	0.08–0.12	0.45–0.75	0.2–0.4	1.05–1.3	0.35–0.65	1.85–2.15	0.1–0.18

Depending on the steelmaking technology, these steels have a bainitic–martensitic structure with finely dispersed Mo, Nb, and V carbides, lath, tempered martensite, lower, upper, and granular bainite. The isotropy of microstructure along the thickness of rolled steel is achieved by complex alloying up to 5%. Among the stronger steels, it is necessary to mention steel F690 with index arc of yield strength not less than 690 MPa and KV<sub>−60</sub> of minimum 80 J.

The analogues of Russian steels for shipbuilding are VL420, VL460, and VL500 offshore steels according to DNVGL-OS-B101 of Rules of DNV GL with KV<sub>−60</sub> of minimum 42, 46, and 50 J, respectively, with a chemical composition of, %: 0.18–0.2 C; 0.1–0.55 Si; 1.6–1.7 Mn; <0.2 Cr; 0.4–0.8 Ni; <0.35 Cu; <0.08 Mo with the O content of 30–50 ppm, as shown in Table 2.

**Table 2.** Chemical composition of steels according to DNVGL-OS-B101, wt%.

Steel	C	Mn	Si	Cr	Cu	Ni	Mo
VL D,EW420, 460, 500	<0.2	<1.7	0.1–0.55	<0.2	<0.35	<0.4	<0.08
VL FW420, 460, 500	<0.18	<1.6	0.1–0.55	<0.2	<0.35	<0.8	<0.08

Shipbuilding steels D,E,FQ43, D,E,FQ47, and D,E,FQ51, according to the Rules of Materials and Welding of American Bureau of Shipping, have a KV<sub>−60</sub> minimum of 41, 46, 51 J, respectively, with the chemical composition, as shown in Table 3.

**Table 3.** Chemical composition of steels according to Rules of Materials and Welding of ABS, wt%.

Steel	C	Mn	Si	Cr	Cu	Ni	Mo
D,E,FQ43 D,E,FQ47	0.14–0.2	1–1.7	0.6–0.8	0.3–2	0.5–0.55	0.8–3.5	0.1–0.7
D,E,FQ51	0.16–0.18	1–1.7	0.6–0.8	0.5–2	0.5–0.55	<3.5	0.5–0.7

Steels for heavy transport and machines are S690QL high-strength martensitic–bainitic steels with a KV<sub>−60</sub> minimum of 27 J according to EN 10025-6, with the chemical composition, %: 0.2 C; 0.6 Si; 1.6 Mn; 0.8 Cr; 0.3 Cu; 2 Ni; 0.7 Mo and S700MC steel with KV<sub>−60</sub> minimum of 40 J according to EN 10149-2 with the chemical composition, %: 0.12 C; 0.25 Si; 2.1 Mn; <0.22 (Nb, V, Ti); 0.015 Al (data of SSAB, Stockholm, Sweden). Analogues are steel 12KhGN2MA (in Russian) with a yield strength of 690 MPa and KV<sub>−70</sub> minimum of 50 J, steel 18KhGNMFR (in Russian) with a yield strength of 950 MPa and KV<sub>−40</sub> minimum of 30 J.

High-strength steels for the pipe industry with strength grades X70, X80, X100, and X120 with an impact energy of KV<sub>0</sub> and a minimum of 27 J, according to API Spec 5L Specification for Line Pipe (USA), have a bainitic and bainitic–martensitic structure and have the chemical composition, %: 0.1–0.12 C; 0.45–0.55 Si; 1.6–2.1 Mn; <0.15 (Nb, V, Ti); <0.5 Cu; <0.5 Ni; <0.5 Cr; <0.5 Mo; <0.004 B. Analogues are pipe steels X70 and

X80, according to GOST ISO 3183-2015 (in Russian) with an impact energy of  $KV_0$  and a minimum of 40 J (data of CHTPZ, Chelyabinsk, Russia) with the chemical composition, as shown in Table 4.

**Table 4.** Chemical composition of steels according to GOST ISO 3183-2015, wt%.

Steel	C	Mn	Si	Cr	Cu	Ni	Mo
X70	<0.12	<1.7	<0.45	<0.5	<0.5	<0.5	<0.5
X80, X100, X120	<0.1	<2.1	<0.55	<0.5	<0.5	<0.5	<0.5

## 2.2. Rail Steels

R260 and R350HT pearlitic rail steels, according to EN 13674-2011, have the strength of 880–1175 MPa and the chemical composition, %: 0.62–0.8 C; 0.7–1.2 Mn; 0.15–0.58 Si; <0.03 V; <0.15 Cr; <0.009 N; <0.004 Al. According to GOST R 51685-2013 (in Russian), rail steels are produced in 13 categories with the tensile strength of at least 900–1280 MPa, at a  $KCU_{-60}$  minimum of 15–25 J/cm<sup>2</sup>. Accelerated cooling, quenching, and tempering are used to produce rail steels. The steels have the chemical composition, %: 0.71–0.95 C; 0.75–1.25 Mn; 0.25–0.6 Si; 0.08–0.15 V; 0.2–1.25 Cr; 0.01–0.02 N; <0.02 S; <0.02 P; <0.004 Al; and elements: Cu, Ni, and Ti, as shown in Table 5.

**Table 5.** Chemical composition of rail steels according to GOST R 51685-2013, wt%.

Steel	C	Mn	Si	Cr	V	Ni	Cu
90KhAF	0.83–0.95	0.75–1.25	0.25–0.6	0.2–0.6	0.08–0.15	<0.2	<0.2
76KhAF	0.71–0.82	0.75–1.25	0.25–0.6	0.2–0.8	0.08–0.15	<0.2	<0.2
76KhF	0.71–0.82	0.75–1.25	0.25–0.6	0.2–0.8	0.08–0.15	<0.2	<0.2
76KhSF	0.71–0.82	0.75–1.25	0.25–0.6	0.5–1.25	0.08–0.15	<0.2	<0.2
90AF	0.83–0.95	0.75–1.25	0.25–0.6	<0.2	0.08–0.15	<0.2	<0.2

The residual content of oxygen is <20 ppm and of hydrogen < 2.5 ppm. Depending on the steelmaking technology, these steels have a pearlitic structure with bainite, martensite, and nonmetallic inclusions. Refining the melt process, micro-alloying, grain refinement, and the improvement of microstructure morphology are used to improve the cold resistance and toughness of pearlitic rail steels [12,13].

As an alternative to pearlitic rail steels, bainite rail steels based on TMCP are successfully developed [14,15]. Low-alloy bainitic rail steels have the chemical composition, %: 0.04–0.5 C; 0.35–2 Mn; 0.25–1.98 Si; 0.1–2.98 Cr; 0.25–0.8 Mo; <0.003 B; <0.1 Nb; <4 Ni; <0.11 Cu; <0.03 Al; <0.03 Ti [16]. Hajizad et al. [17] proposed the TMCP diagram of B360-HT bainitic rail steel, %: 0.269 C; 0.51 Cr; 1.547 Mn; 1.36 Si; 0.033 V; 0.148 Mo; 0.006 N with the tensile strength of 1879 MPa. According to the TMCP diagram, the process consists of heating to 900 °C with a holding time of 600 s, accelerated cooling from 900 °C at cooling rate of 50 °C/s, holding time of 3600 s at 330 °C, and accelerated cooling in a salt bath.

Liu [18] presented the CCT diagram for of Q345C micro-alloyed bainitic rail steel for high-speed railroads in China, %: 0.138 C; 0.292 Si; 1.333 Mn; 0.006 P; 0.001 S; 0.005 Cu 0.006 Ni; 0.012 Cr; 0.002 V; 0.013 Nb; 0.022 Al; 0.011 Ti and proved that the microstructure of the steel includes perlite (P), ferrite (F), bainite (B), and martensite (M) at a  $t_{8/5}$  cooling time of 6000–3 s with a hardness of 160–405 HV.

## 2.3. Duplex Steels

Duplex steels are classified into two groups: low 0.01–0.08% and high 0.3–0.5% carbon content. The composition of duplex steels includes, %: <2.5 Mn; <2 Si; 18–28 Cr; 2.5–8 Ni; 1–4 Mo; 0.05–0.33 N; <2.5 Cu [19], as shown in Table 6.

**Table 6.** Chemical composition of low carbon duplex and superduplex steels, wt%. Data from [19].

Steel	C	Mn	Si	Cr	Ni	Mo	Cu	N
2304	0.03	2.5	1	21.5–24.5	3–5.5	-	0.05–0.6	0.05–0.2
Uranus 50	0.04	2	1	20.5–22.5	5.5–8.5	2–3	1–2	0.2
2205	0.03	2	1	22–23	4.5–6.5	2.5–3.5	-	0.08–0.2
44LN	0.03	2	1	24–26	5.5–6.5	1.2–2	-	0.14–0.2
DP3	0.03	1	0.75	24–26	5.5–7.5	2.5–3.5	0.2–0.8	0.1–0.3
329	0.08	1	0.75	23–28	2.5–5	1–2	-	-
2507	0.03	1.2	0.8	24–26	6–8	3–5	0.5	0.24–0.32
Zeron 100	0.03	1	1	24–26	6–8	3–4	0.5–1	0.2–0.3
DP3W	0.03	1	0.8	24–26	6–8	2.5–3.5	0.2–0.8	0.24–0.32
AF918	0.025	-	0.8	24–26	6.5–8	3–4	1.2–2	0.23–0.33

Duplex steels have balanced alloying for equal volume fractions of ferrite and austenite, which provides optimal mechanical properties and high resistance to intergranular and stress corrosion. Duplex steels have higher strength and viscoplasticity than ferritic steels. The tensile strength reaches 620–1000 MPa and elongation is at least 15–30%, with high impact toughness to minus 45–70 °C.

The problem with duplex steels is embrittlement, which is divided into types: embrittlement due to carbide network, especially in austenite and in high carbon alloys; embrittlement due to  $\alpha'$ -phase formation or 475 °C ferrite embrittlement; embrittlement due to  $\sigma$ -phase formation, especially in ferrite. The study of super duplex steel 2510 SDSS, %: 0.02 C; 0.44 Si; 0.37 Mn; 25.3 Cr; 9.9 Ni; 4 Mo; 0.018 P; 0.001 S; 0.275 N showed a significant effect of Cr, Mo, W, and Si on Time Temperature Transformation (TTT) and on the formation of dispersed phases:  $M_7C_3$ ,  $M_{23}C_6$ ,  $Cr_2N$ ,  $CrN$ ,  $\delta$ -,  $\sigma$ -,  $\chi$ -,  $\gamma_2$ -,  $\pi$ -, and  $\epsilon$ -,  $\alpha'$ -phases [20]. Duplex steels have excellent mechanical properties at low temperatures, as shown in Figure 6.

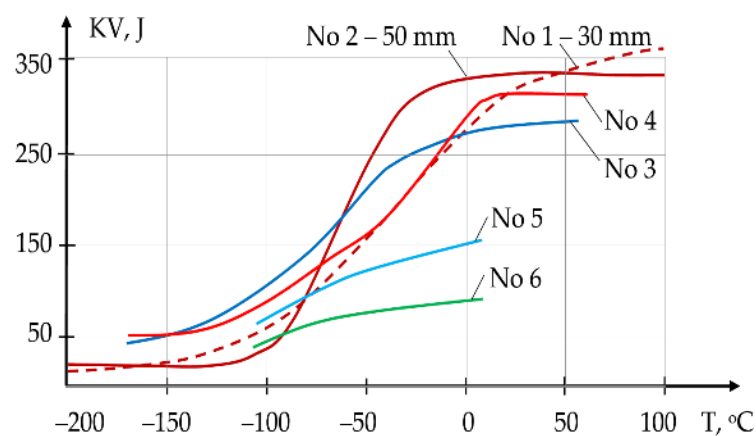


**Figure 6.** Impact energy at low temperatures: No. 1—SAF 2205 30 mm; No. 2—SAF 2205 50 mm. Data from [21]; No. 3—SAF 2205, No. 4—SAF 2507, No. 5—TIG-welding of SAF 2507. Data from Sandvik Materials Technology; No. 6—EB-welding of SAF 2205. Data from [22].

#### 2.4. High-Manganese Cryogenic Steels

High-manganese cryogenic steels have excellent viscoplasticity and mechanical properties at low temperatures. Weldability depends on the welding thermal cycle, initial microstructure, and chemical-heterogeneity of grain boundaries. Simulation of thermal cycles for Mn-steel, %: 0.43 C; 0.2 Si; 23.8 Mn; 4.2 (Cu + Cr) with the tensile strength of 810 MPa, elongation of 45%, and  $KV_{-196}$  of 201 J showed that the steel has a high impact energy of 163–204 J at a temperature of minus 196 °C [23]. For steels, %: 20 Mn; 4 Al; 0.3 C and 27 Mn; 4 Al; 0.3 C, the tensile strength is 660–1196 MPa, elongation is 49–77%, and the impact energy  $KV_{-196}$  is 100–180 J [24]. The alloying of 0.3–0.6% of V in the steel, %: 0.58 C; 0.5 i; 23 Mn; 1.9 Al at +20 °C leads to a change in the tensile strength from 804 to 867 MPa and elongation from 62% to 57% [25]. At the test temperature minus 196 °C, the strength changes from 1409 to 1527 MPa, elongation from 75% to 60%, and the impact

energy  $KV_{-196}$  from 155 to 121 J. The alloying of 1% of nickel or copper into 22 Mn-0.45 C-1 Al-steel at minus 196 °C leads to a slight decrease in the strength from 1375 to 1322 MPa, to an increase in elongation from 79% to 87%, and to an increase in impact energy  $KV_{-196}$  from 118 to 133 J [26].

### 2.5. High-Entropy Alloys

Advanced high-entropy alloys, an alternative to cryogenic steels, have the highest plasticity at low temperatures and in cryogenic service in corrosive environments. HEA theory is based on thermodynamic modeling. The entropy of HEA increases with the number of alloying elements. High-entropy alloys have five or more alloying elements with content from 5 to 35 at. pct [27,28]. HEAs are classified as single-phase, multiphase, and amorphous with low and high densities of 2.6–6.7 g/cm<sup>3</sup> with the maximum tensile strength of <1500 MPa and elongation of <75% [29,30]. The mechanical properties of HEA are superior to cryogenic nickel alloys and austenitic steels [31]. The metallurgy, weldability, and welding technologies of HEA are developing intensively [27,28].

### 2.6. Austenitic and Superaustenitic Steels

Traditional austenitic steels have the composition, %: 0.02–0.08 C; 1–2 Mn; 0.5–3 Si; 16–25 Cr; 8–20 Ni; <2 Mo; <0.16 N, as shown in Table 7.

**Table 7.** Chemical composition of austenitic and superaustenitic steels, wt%. Data from [32].

Steel	C	Mn	Si	Cr	Ni	Mo	Others
304	0.08	2	1	18–20	8–12	-	-
308	0.08	2	1	19–21	10–12	-	-
316	0.08	2	1	16–18	10–14	2–3	-
321	0.08	2	1	17–19	9–12	-	0.7 Ti
347	0.08	2	1	17–19	9–13	2–3	1 Nb
316LN	0.02	1	0.4	17	13	2.2	0.13 N
317LMN	0.02	1	0.4	18.5	15.5	4.5	0.16 N
Nitronic 30	0.02	8	0.5	16	2.25	-	0.23 N
Nitronic 32	0.08	18	0.5	18	-	1	0.5 N; 1 Cu
Nitronic 40	0.04	9	0.5	20	6.5	-	0.28 N
Nitronic 50	0.04	5	0.4	22	12.5	2.25	0.3 N; 0.2 Nb
254SMo	0.01	0.5	0.4	20	18	6.25	0.2 N; 0.75 Cu
AL-6XN	0.02	1	0.5	21	24.5	6.5	0.22 N

The high-manganese austenitic steels have the composition, %: 0.02–0.15 C; 0.5–4 Si; 5–18 Mn; 16–22 Cr; <12.5 Ni; <3.5 Mo; 0.13–0.5 N. Superaustenitic steels have the composition, %: 0.01–0.02 C; 0.5–1 Mn; 0.4–0.5 Si; 20–25 Cr; 15–25 Ni; 4–8 Mo; 0.2–0.6 N. Austenitic and super-austenitic steels have excellent viscoplasticity, mechanical properties at cryogenic temperature, and corrosion resistance in different aggressive environments. The problem of weldability of austenitic steels is high sensitivity to the welding thermal cycle, grain growth, and hot cracking. Another problem is nitrogen porosity and losses in nitrogen content, especially in laser and beam welding [32].

### 3. Properties of Advanced High-Strength Steels

Metallurgical innovations are implemented in the development and production of advanced high-strength steels [33,34]. AHSS production is based on TMCP [35,36]. The models and technologies for AHSS are aimed at the automotive industry, therefore, the steels are up to 4 mm thickness. However, the thermophysical-mechanical principles of TMCP, thermodynamic models, and metallurgical technologies of AHSS-making can be applied to steelmaking of higher thicknesses.

Advanced high-strength steels have strengths of more than 500 MPa and a complex microstructure of ferrite, martensite, bainite, and residual austenite [37]. The first generation of AHSS includes dual-phase DP steels with F-M microstructure with the tensile

strength of up to 1400 MPa, complex phase CP steels with F-B + P-M-A microstructure with a tensile strength of up to 1300 MPa, martensitic steels with the tensile strength of up to 1600 MPa, TRIP steels with induced plasticity at martensitic transformation of residual austenite during the plastic deformation with F-M/B + A, and a microstructure with the tensile strength of up to 1000 MPa [38]. The second generation includes austenitic high-manganese TWIP steels with induced plasticity through twinning with the tensile strength of up to 1650 MPa, lightweight L-IP steels with induced plasticity with the tensile strength of up to 1150 MPa, and supraustenitic high-manganese steels with the tensile strength of up to 1150 MPa with elongation of up to 60%. The third generation of AHSS includes ultra-high-strength Mn-TRIP steels, Q&P steels with martensitic-austenitic microstructure, and ultra-high-strength carbide-free CFB steels.

### 3.1. Dual-Phase Steels

Dual-phase steels have a ferrite matrix and 10–40% of the martensite volume fraction. The tensile strength of DP steels is 500–1200 MPa, and the elongation is up to 30%. The typical chemical composition of DP steels includes, %: 0.08–0.18 C; 1.6–2.4 Mn; 0.4–0.7 Si, as well as micro-alloying with the elements: Al, Mo, Cr, B, Nb, V, and P, as shown in Table 8.

**Table 8.** Chemical composition of dual-phase steels, wt%. Data from [37].

Steel	C	Mn	Si
DP 450	0.08	1.6	0.4
DP 500	0.14	1.6	0.4
DP 600	0.14	2.1	0.4
DP 780	0.17	2.2	0.6
DP 980	0.11	2.9	0.7
DP 1180	0.18	2.4	0.6

The kinetic transformations in DP steels depend on the alloying system [39]. DP steels have an extremely high impact toughness at low temperatures. Cao et al. [40] studied a DP steel with the chemical composition, wt. %: 0.05–0.2 C; 5 Mn; 3–4 Al with the tensile strength of 1000–2000 MPa at impact energy  $KV_{-40}$  of 50–450 J. Mazaheri et al. [41] proposed the TMCP diagram of DP steel, %: 0.17 C; 0.4 Si; 1.15 Mn; 0.95 Cr; 0.035 S; 0.025 P with the tensile strength of 850–1400 MPa and elongation of up to 15%. According to the TMCP diagram, the process consists of heating to 880 °C with a holding time of 3600 s, accelerated cooling from 880 °C to 770 °C, holding at 770 °C with a time of 6000 s, rolling at room temperature, heating to 790 °C with a holding time of 600 s with accelerated cooling, as shown in Figure 7a.

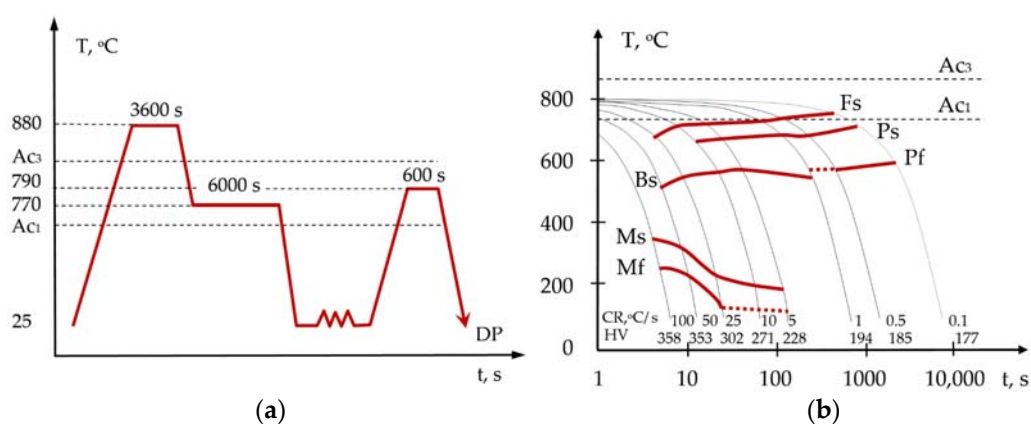


**Figure 7.** (a) TMCP diagram of DP steel. Data from [41]. (b) CCT diagram of DP steel. Data from [42]. Index s is start; index f is finish.

Bräutigam-Matus et al. [42] presented the typical CCT diagram during cooling from 800 °C on the basis of dilatometric curves of DP steel, %: 0.18 C; 1.80 Mn; 0.015 P; 0.002 S; 0.007 N; 0.33 Si; 0.08 Cu; 0.05 Ni; 0.43 Cr; 0.03 Nb; 0.015 Mo; 0.026 Ti; 0.004 V; 0.0007 B and proved that the microstructure of the DP steel includes perlite (P), ferrite (F), bainite (B), and martensite (M) at a cooling rate of 0.1–100 °C/s < of 177–358 HV, as shown in Figure 7b.

### 3.2. TRIP Steels

TRIP steels contain 0.1–0.4% C and alloying elements Si, Al, Ti, Ni, V. The typical composition of TRIP is 590, 690, 780, wt. %: 0.175–0.25 C, 2 Mn, 2(Al + Si) [37], as shown in Table 9.

**Table 9.** Chemical composition of TRIP steels, wt%. Data from [37].

Steel	C	Mn	Al + Si	Al + Mn	Si + Cr + Mo
TRIP 590	0.175	2	2	-	-
TRIP 690	0.2	2	2	-	-
TRIP 780	0.25	2	2	-	-
TRIP 700	0.2	-	-	2.9	0.4

The typical composition of TRIP 600, 700, 800, wt. %: 0.15–0.25 C, 1.5 Mn, 1.5(Al + Si), <0.5(Cr + Mo), <0.05(Ti + Nb), <0.006 N, <0.04 P, <0.01 S [43]. Aluminum alloying increases plasticity and elongation up to 18–38%; alloying C, Cu, Si, and Nb reduces plasticity but increases the tensile strength up to 600–800 MPa.

The microstructure consists of a ferritic or bainitic matrix and a 5–20% volume fraction of metastable residual austenite, which transforms into martensite during plastic deformation. High plasticity allows the use of TRIP steels in bending and stamping, which is important for the automotive industry. Martensitic transformation during deformation occurs at a high rate, which is important for the strength of the auto body under impact load. Unlike DP steels, the microstructure of TRIP steel has bainite and residual austenite, which transforms into martensite during deformation.

Wu et al. [44] proposed the TMCP diagram of TRIP steel, %: 0.233 C, 1.365 Si, 1.54 Mn, Al 0.080, 0.004 S, 0.007 P with the tensile strength of 824 MPa and elongation of 37%. According to the TMCP diagram, the process consists of heating to 1120 °C with austenization, slow cooling from 1120 °C to 840 °C with multistage rolling at 1060, 1000, 920, and 840 °C, and accelerated water-cooling. Grajcar et al. [45] presented the typical CCT diagram of TRIP steel, %: 0.24 C, 1.55 Mn, 0.87 Si, 0.4 Al, 0.034 Nb, 0.023 Ti and proved that the microstructure of the TRIP steel includes perlite (P), ferrite (F), bainite (B), and martensite (M) at a cooling rate of 1–298 °C/s with a hardness of 232–482 HV.

### 3.3. Complex Phase Steels

Complex phase (CP) steels have an ultradispersed ferritic–bainitic microstructure with a small amount of martensite, residual austenite, and pearlite. These steels contain less than 0.25% C as well as alloying elements similar to TRIP and DP steels, but additionally have minor alloying with Nb, Ti, and V for dispersion strengthening, as shown in Table 10.

**Table 10.** Chemical composition of CP steels, wt%. Data from [37].

Steel	C	Mn	Si
CP 600	0.1	1.6	0.4
CP 800	0.1	2	0.25
CP 1000	0.18	2.4	0.6
CP 750	0.25	1.4	0.4
MS 1200	0.15	1.5	0.25

Typical hot-rolled steel CP 800, %: 0.1 C; 2 Mn; 0.25 Si contains 42% of ferrite, 40% of bainite, 13% of martensite, and 5% of residual austenite. The tensile strength is 800–1300 MPa with elongation of up to 35%. Mesplont [46] proposed the TMCP and CCT diagram of CP steel, %: 0.14 C; 1.72 Mn; 0.0285 Ti; 0.0035 B; 0.005 N with the tensile strength of 800–1300 MPa and elongation of 14–24%. According to the TMCP diagram, the process consists of heating to 1270 °C with a holding time of 3600 s, hot rolling at a temperature of 1150–850 °C, accelerated cooling from 850 °C to 550 °C, and slow cooling from 550 °C to room temperature. According to the CCT diagram, the microstructure of DP steel includes perlite (P), ferrite (F), bainite (B), acicular ferrite (AF), and martensite (M) at a cooling rate of 0.1–25 °C/s [46].

### 3.4. Superaustenitic Manganese Steels

Superaustenitic manganese steels contain, %: 0.01–0.15 C; 0.5–18 Mn; 0.13–0.5 N; 0.4–4 Si; <1 Cu; 5–24 Ni; 16–22 Cr; <0.2 Nb; 1–6 Mo. Zhang et al. [47] presented thermodynamic modeling of UNS S32654 steel (654 SMO), %: <0.02 C; 2–4 Mn; 0.45–0.55 N; 0.5 Si; 0.3–0.6 Cu; 21–23 Ni; 24–25 Cr; 7–8 Mo. The stable phases in the austenitic matrix of this steel are:  $M_{23}C_6$ ,  $Cr_2N$ ,  $\sigma$ -phase. The metallurgy, weldability and welding technologies of Mn-steels are developing intensively [47].

### 3.5. TWIP Steels

TWIP steels have an austenitic structure and high manganese content, %: 22–31 Mn; 0.9–4.1 Al; 0.2–0.55 Si; 0.01–0.17 C; <1(Cr + Mo); <0.05 Nb, as shown in Table 11.

**Table 11.** Chemical composition of TWIP steels, wt%. Data from [37].

Steel	C	Mn	Si	Cr + Mo	Al	Nb
TWIP 1	0.08	28	0.28	<0.01	1.6	<0.001
TWIP 2	0.08	25	0.24	<0.01	1.6	0.05
TWIP 3	0.08	27	0.52	<0.01	4.1	0.05
TWIP 4	0.17	28.1	0.54	<0.01	0.9	<0.001
TWIP 5	0.11	23.9	0.448	1	3.5	<0.001
TWIP Fe-24Mn	0.0163	24.3	-	-	-	-
TWIP Fe-30Mn	0.0163	30.79	-	-	-	-

TWIP steels have the tensile strength of up to 900–1000 MPa, elongation of up to 50–60%, and a lower density due to Mn and Al. TWIP steels are divided into two groups: without carbon and with carbon. Modeling of TWIP steel, %: 27.36 Mn; 0.09 C 3 Al; 1.92 Si; 1.73 Cr; 0.85 Ni; 0.29 Mo; 0.2 Cu; 0.03 Ti; 0.018 B; 0.02 S; 0.012 N showed the presence of various phases:  $M_{23}C_6$ , M (C, N),  $MB_2C_{32}$ ,  $M_3B_2$ ,  $M_3B_2$ ,  $Ti_4C_2S_2$ , and inclusions of AlN and MnS [48]. Demeri [37] presented the typical thermal cycles of TMCP for TWIP Fe-24Mn steel. According to the TMCP diagram, the process consists of heating to 900 °C with a holding time of 7200 s, slow cooling from 900 °C to 25 °C, and accelerated cooling in dry ice at the minus 78.5 °C or liquid nitrogen (N) at the minus 195.7 °C with a holding time of 3600 s, as shown in Figure 8.

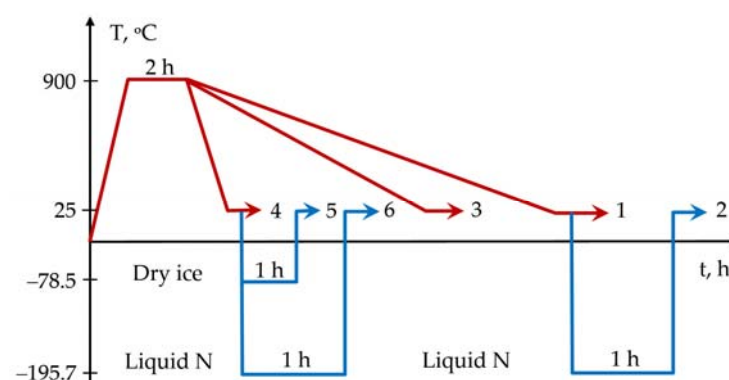


**Figure 8.** Thermal cycles for TWIP Fe-24 Mn steel. Data from [37].

### 3.6. Mn-TRIP—Steels

Mn-TRIP are cryogenic medium manganese steels with 4–10% Mn content belongs to promising ultra-high-strength steels of the third generation weldability research, which is at the beginning. Mn-TRIP steels have high residual austenite content, elongation of at least 25%, and tensile strength range of up to 1000–1700 MPa, and a high impact energy due to TMCP and complex micro-alloying with elements C, Ni, Si, Al, N, and B, as shown in Figure 9.

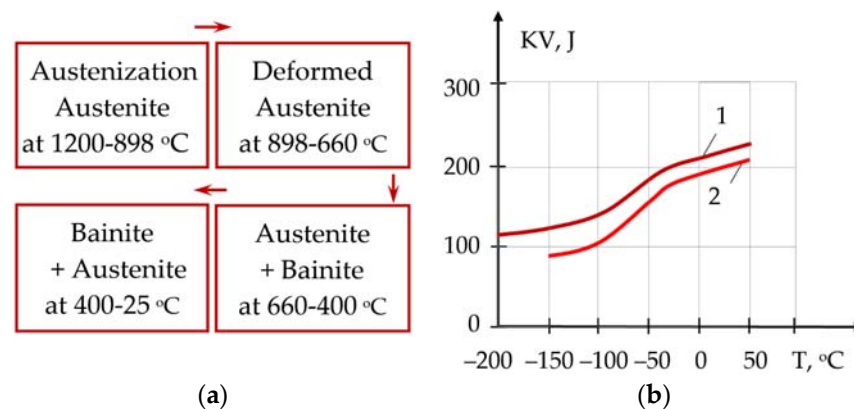


**Figure 9.** (a) TMCP diagram of Mn-steel. Data from [49]; (b) impact energy for medium manganese steel: (1) medium manganese steel, %: 7.22 Mn; 0.093 C; 0.49 Si; 0.013 Al; 0.005 P; 0.007 S. Data from [50]; (2) medium manganese steel, %: 0.04 C; 0.12 Si; 4.87 Mn; 4.98 Ni; 0.0047 S; 0.011 P; 0.03 Nb. Data from [51].

Kozłowska et al. [49] presented the typical TMCP diagram of Mn-steel, %: 0.16 C-4.7 Mn-1.6 Al-0.2 Si. According to the TMCP diagram, the process consists of heating to 1200 °C with an austenization, slow cooling from 1200 °C to 660 °C with multistage hot rolling at 1050, 898, and 660 °C, and accelerated cooling from 660 to 400 °C for the formation of bainite, holding time of 300 s at 400 °C, and slow cooling from 400 °C to 25 °C for the formation of bainite–austenite microstructures.

### 3.7. Q&P Steels

To produce Q&P steels with martensitic–austenitic microstructure, full or partial austenization is used. Initial martensite is produced by quenching austenite or a mixture of austenite and ferrite below the  $M_S$  temperature with equal carbon volume content in martensite and austenite. As a result of isothermal one- or two-step holding, the residual austenite is gradually enriched in carbon. The basic concept of the Q&P process involves separation of carbon by diffusion across the martensite/austenite interface to stabilize the residual austenite, as shown in Figure 10.

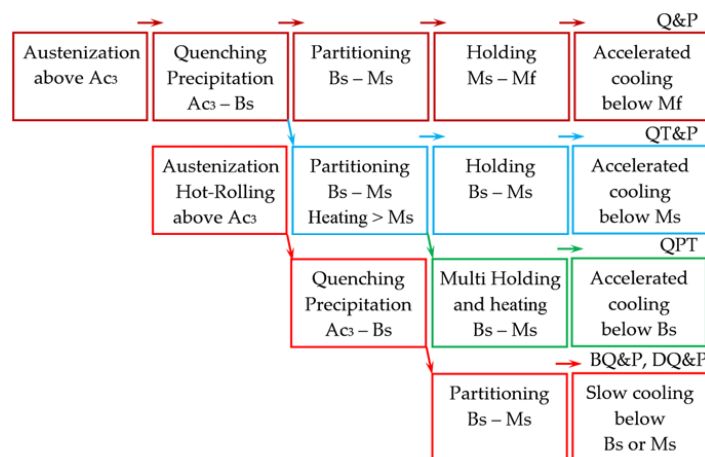


**Figure 10.** Diagrams of TMCP: quenching and partitioning (Q&P); quenching-tempering and partitioning (QT&P); quenching-partitioning-tempering (QPT); non-isothermal direct quenching and dynamic partitioning (DQ&P); non-isothermal (BQ&P). (Bs) is bainite transformation start; (Ms) is martensite transformation start; (Mf) is martensite transformation finish. Data from [52,53].

A new method of asymmetrical thermomechanical processing of Q&P steel, %: 0.2 C; 1.5 Mn; 1.3 Si; 0.2 Al allowed achieving a tensile strength of up to 1023 MPa, with elongation of 35% [54]. Especially important when introducing ultra-high-strength Q&P steels is the effect of hydrogen embrittlement, due to the high hydrogen solubility in the austenitic matrix and high diffusion coefficient in martensite. This complex effect negatively affects the cold resistance of welded joints and requires further study [55].

### 3.8. CFB Steels

Carbide-free bainitic (CFB) steels are extra-high-strength TRIP steels with lath bainitic ferrite in residual austenite without carbides. An increase in strength and plasticity is achieved due to the ultradispersity of the bainitic ferrite plates and the TRIP effect. The strength of CFB steels reaches 1200–2000 MPa with elongation of 10–25%. The elements used for complex alloying, %: 0.3–0.98 C; <2 Mn; <3.5 Si; <1.5 Cr; <1 Co; <1 W, as well as Al, Ti, Cu, V, Mo, N, and B. [56,57]. Chen et al. [58] proposed the TMCP and CCT diagram of CFB steel, %: 0.25 C; 1.54 Si; 1.84 Mn; 0.23 Mo; 0.032 Nb; 0.019 Ti; 0.51 Cr; 0.14 Cu; 0.0025 B; 0.0028 N with a tensile strength of 1298 MPa. According to the TMCP diagram, the process consists of heating to 115 °C with a holding time of 300 s, hot rolling at a temperature of 1050 and 900 °C, and slow cooling from 900 °C to room temperature at a cooling rate of 0.05–10 °C/s, as shown in Figure 11a.

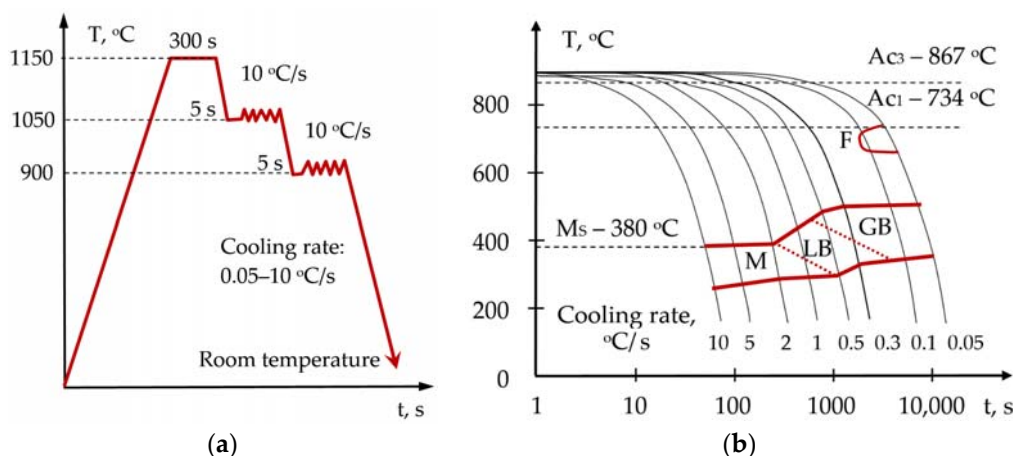


**Figure 11.** (a) TMCP and (b) CCT diagram of CFB steel. Data from [58].

According to the CCT diagram, the microstructure of CFB steel includes ferrite (F), grain boundary ferrite (GB), lath bainite (LB), and martensite (M) at a cooling rate of 0.05–10 °C/s, as shown in Figure 11b.

#### 4. Problem of Fracture of Steels at Low Temperatures

The main tasks in manufacturing welded structures for low temperature services are to increase reliability and durability and reduce weight and cost. Relevant tasks are increasing the viscoplasticity of steels, reducing the sensitivity to embrittlement and hydrogen cracking, and increasing the cyclic loads at low temperatures. Pous-Romero [59] studied the critical temperature of ductile-brittle transition and the ductile fraction in low-temperature tests of ASTM SA508 Gr.3 low-alloy hull steel, %: <0.25 C; 1.2–1.5 Mn; 0.45–0.6 Mo; 0.4–1 Ni; <0.25 Cr; 0.15–0.35 Si and proved that the impact energy decreases from 230 J at plus 50 °C to 120 J at a critical temperature of minus 50 °C and to 10 J at minus 100 °C with 0% of ductile fracture.

Most fractures in steels occur during the formation and propagation of cracks initiating in local stress concentrations, in dislocation clusters, and at intergranular and interphase boundaries, as well as at nonmetallic sharp-edged shape inclusions [60].

Brittle fractures typically involve little energy absorption and occur by splitting (chipping) as the crack propagates through the atomic plane. Ductile fractures occur during formation of microporous coalescence, in which the initiators of fracture are dispersed inclusions and carbides distributed in the viscous matrix. Decohesive fractures occur during the microfracture along grain boundaries, which have a lower strength than the grain. A decrease in the strength of intergranular boundaries occurs during segregation of brittle and harmful impurities, as well as during the corrosive influence.

The effect of temperature on impact toughness is determined by Charpy tests. Fracture toughness decreases with a temperature reduction and the occurrence of an embrittlement of steels. The brittle fracture of steels occurs at a critical low temperature in the ductile-brittle transition temperature range. A significant number of physical and analytical models have been developed to describe fracture micromechanics [61]. Microstructural factor, volume, size, and distribution of dispersed phases, intermetallics, nonmetallic inclusions, impurities of S, P, absorption of H, O, N, diffusion of H, S, C, and phase transformations during heat input in welding and heat treatment are important in the models and mechanisms of fractures.

##### 4.1. Hydrogen Embrittlement of Steels

The term “Hydrogen Embrittlement” refers to a sharp decrease in the viscoplasticity of materials under the influence of hydrogen. A characteristic feature of hydrogen embrittlement is the reduction of maximum elongation and reduction in the area in mechanical static tensile testing of samples. It is important to note that embrittlement is not detectable by Charpy tests because the hydrogen embrittlement mechanism is activated at a certain ratio of hydrogen atom diffusion rate and rate of dislocation motion.

Hydrogen embrittlement and hydrogen-assisted cracking (HAC) is a serious problem in welded structures made of bainitic, martensitic, ferritic, and duplex steels [62,63]. Hydrogen embrittlement and cracking also occurs in austenitic chromium-nickel steels during the long-term operation of vessels under pressure in hydrogen-containing media, at pressures from 140 to 240 atm [64,65]. AHSS also exhibit high sensitivity to hydrogen embrittlement, thus this effect requires further study [66].

A complex phenomenon in DP and TRIP steels for welded structures for low temperature and cryogenic service is the effect of plasticity reduction under the influence of hydrogen [67]. Begic Hadipasic et al. [68] found a decrease in elongation under the influence of hydrogen in DP steel from 24% to 20% and in TRIP steel from 45% to 30%. These data are confirmed in tests of TRIP-800 steel [69,70]. TWIP steels also show high sensitivity to hydrogen embrittlement. A study of the steels, %: 18 Mn-0.6 C and 18 Mn-1.2 C showed a decrease in elongation from 70% to 32% at hydrogen charging [71]. Cryogenic

nickel alloys for liquid gas storage are also subject to hydrogen embrittlement, especially when alloyed with hydride-forming elements: Ti, Zr, V, Nb, La, Ce, and Th [72].

All welded structures for low temperature and cryogenic service are subject to hydrogen-containing corrosion. Welded joints absorb hydrogen from coated electrodes, flux-cored wires, welding fluxes, oxide layers, shielding gases, and high atmospheric humidity. During welding, water and molecular hydrogen dissociate into atoms in the plasma, which are actively adsorbed on the surface of the weld pool. After metal crystallization, hydrogen is absorbed in the weld metal and forms solid interstitial solutions with the crystal lattice of the ferrite and austenite matrix. Hydrogen can easily diffuse through crystalline microstructures because it has a small atomic radius.

HAC occurs in the microstructure after a critical level of local yield stress, which sharply decreases with diffusible hydrogen content. Therefore, when modeling the HAC mechanism, the mutual influence of three factors is considered: local hydrogen concentration, local stress, and local microstructure [73,74].

#### 4.2. Mechanisms of Hydrogen Embrittlement

One of the first adsorption mechanisms of hydrogen embrittlement was developed in 1928 by the Academician of the USSR Academy of Sciences P.A. Rehbinder. Based on the Rehbinder effect, the Hydrogen-Enhanced Decohesion (HEDE) mechanism was developed. HEDE is based on the reducing of the decohesion energy and stress for the tip opening crack with a critical concentration of diffusible hydrogen [75–77], as shown in Figure 12.

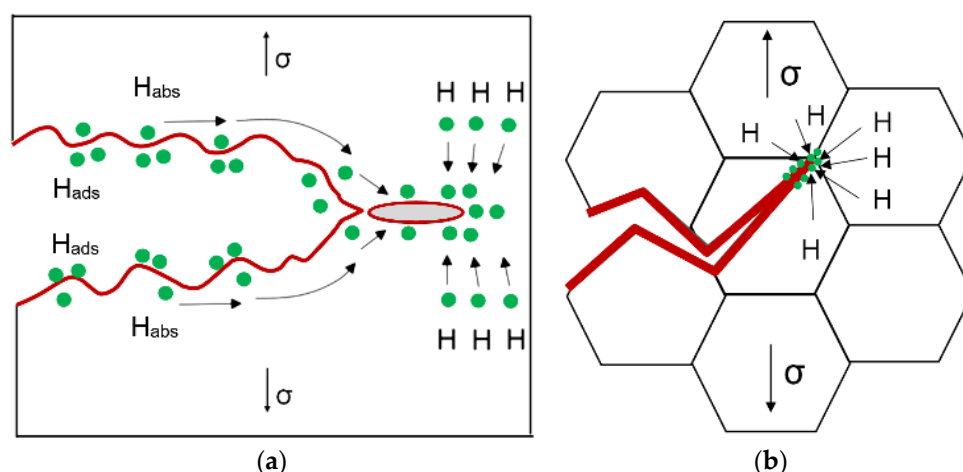


**Figure 12.** Diagram (a) of crack development according to the HEDE theory with hydrogen traps under stress corrosion; diagram (b) of the HELP mechanism of crack growth under the influence of diffusible hydrogen and local plastic deformation at the crack tip. Data from [78].

The Hydrogen-Enhanced Local Plasticity (HELP) mechanism, which was developed in the studies of Sofronis, Birnbaum, and Lynch, was a significant advance in the micromechanics of hydrogen embrittlement [79–81]. According to the HELP mechanism, hydrogen in solid solution blocks elastic interactions and stresses, which promotes the movement of dislocations and increases local plasticity. The Adsorption-Induced Dislocation Emission (AIDE) mechanism or the theory of dislocation movement under the influence of hydrogen adsorption was developed by Lynch [81] and in nonlinear long-wavelength models of concentration of hydrogen by Polyanskiy, Belyaev, and Porubov [82,83].

### 5. Improvement of Viscoplasticity of Steels

Theoretical foundations for improving the viscoplasticity of steels are based on the studies by R. Hadfield, J. Chipman, A. Samarin, A. Baikov, E. Bain, A. Cottrell, H. Bhadeshia, N. Liakishev, and I. Gorynin [84–87]. TMCP and the formation of nonmetallic inclusions leads to residual stresses at the interface between the inclusion and the steel matrix, due to

different coefficients of thermal expansion and mechanical properties. The local stresses in the nonmetallic inclusions of Mg-Al-O, Al-Ca-O-S, and TiN, especially with sharp-edged shapes, can reach 750–2000 MPa, which leads to the fracture of brittle inclusions and the appearance of cracks [88].

As shown by the Electron Backscatter Diffraction (EBSD) analysis, parameters of TMCP and the hardening of Cu-containing HSLA steels can lead to coagulation and irregular distribution of Cu precipitates. This reduces the isotropy of rolled steel and the weldability of high-strength steels, especially with errors in welding parameters [89]. The composition, morphology, and micromechanical properties of nanoparticles smaller than 1 nm, including Cu precipitates, NiAl, Ni<sub>2</sub>AlMn, Ni<sub>2</sub>AlTi, Ni<sub>3</sub>Ti, NbC, and Mo<sub>2</sub>C intermetallics should be considered to improve impact toughness at low temperatures and weldability. For the isotropy of high-strength steels, the development of a synergistic combination of nanoparticles in the nanoscale hardening mechanism is required [90].

Reducing the ductile-brittle transition temperature to minus 120 °C and improving the weldability of high-strength cold-resistant steels can be achieved through developing methods of the microstructural design of rolled products and welded joints based on X-ray microstructure tomography [91,92]. An important field is the physical thermomechanical modeling to build CCT diagrams to determine the optimal concentrations of alloying elements, Cr, Nb, V, Ni, Ti, Mo, and N [93]. An increase in the viscoplasticity of steels is also achieved through the refinement of the primary austenitic grain, through the control of solubility and distribution of dispersion carbides, nitrides, and complex carbonitrides, VC, VN, TiC, TiN, Nb (C, N), and NbTi (C, N) [94,95].

Optimization of the TMCP of austenitic cold-resistant stainless steels, application of cold rolling, and annealing for grain refinement have great potential for the improvement of viscoplasticity. The application of the TMCP reversion method for AISI 304L ultradisperse steel [96–98] allowed achieving a tensile strength of 1010–1640 MPa with an elongation of 40–59% and excellent weldability during laser welding. High mechanical properties have products made of AISI 316L cryogenic steel from SLM (Selective Laser Melting) technology. The tensile strength of SLM samples at a temperature of minus 196 °C reached 1355–1510 MPa with an elongation of 35–54% [99].

The key importance for the development of AHSS is the study of hardening mechanisms, the determination of dependence between dispersive precipitations and microstructure refinement, studies of thermodynamics, solubility, and crystallography of precipitations [100]. The future development of second- and third-generation ANSS is connected to the development of the mechanisms of nanometer hardening, synergistic effect of dispersion precipitations, and volume isotropy of rolled steel [101]. The solution to these problems is possible through the application of neural network technologies in material science and metallurgy [102,103].

## 6. Weldability of High-Strength Steels

Laser welding of boron-containing ultra-high-strength steel Docol PHS CR 2000 leads to the formation of a softening layer in the heat-affected zone (HAZ) when heating in the temperature range  $Ac_1$ – $Ac_3$ . The microstructure of this layer consists of tempered martensite, and tensile strength is 33% lower compared to that of the base metal [104]. In addition to the softening effect, a hardening effect may occur in the HAZ. During hybrid laser-arc welding of S960QL steel, the hardness in HAZ increases to 436 HV with 383 HV in the weld metal and 350 HV in the base metal [105].

Kang et al. [106] studied the MAG welding of DP590 GA, SAE 1008, HSLA HR 420, DP600 HR, Boron, Boron-HSLA, DQSK, TRIP780 GI, and DP780 GI steels and dissimilar joints. Typical weld fractures during cyclic tests occur along the weld metal, in HAZ, and in areas of high stress concentration. Steel thickness, stress concentrators in the structure, and the shape of the welds have a significant influence on the fracture of samples during cyclic tests. The main problem in the welding of DP steels is also the hardening and softening effect in the heat-affected zone. During laser welding of 0.15C-1.7Mn-steel, softening

in the low-temperature HAZ (LT-HAZ) reached 20% due to martensite tempering. In the high-temperature HAZ (HT-HAZ), strength increased up to 28% due to martensite formation compared with base metal [107]. Formation of a martensitic layer near the weld metal and softening results in fractures under static, impact, and cyclic dynamic loads. As the tensile strength of DP steel increases up to 1000 MPa, the softening increases up to 25–78% [108–110]. During laser welding of DP 980, the softening layer strength decreases by 41%, which is the main cause of fractures under cyclic and vibration loads [111].

To control the welding thermal cycle and microstructure of DP 590 steel, the change in laser pulse frequency can be used [112]. Twin-spot laser welding is used to reduce the cooling rate and hardening when welding DP, CP, and TRIP steels [113,114]. Changing the ratio of power of two laser beams allows one to optimally distribute the heat input, reducing the width of HAZ, the volume of martensite, and the weld hardness by 10%. These effects are important for improving the isotropy of welded joints. Martin-Root [115] investigated the laser welding of CP 980 steel. The hardness in the HT-HAZ increased from 460 to 520 HV.

Laser, arc, and resistance welding are also promising for welding TWIP steels [116–119]. The problem of Mn-TWIP steels is also high sensitivity to the welding thermal cycle. This results in weld metal softening of up to 20–40%, due to microstructural phase transformations [120,121], and a softening of up to 35% in HAZ [122]. Ma et al. [122] performed the TIG and laser welding of 25 Mn-3 Al-3 Si steel. The weld hardness during TIG welding increased to 360 HV and during laser welding to 420 HV with the base metal hardness of 320 HV. The HAZ hardness during TIG welding decreased to 230 HV and during laser welding to 290 HV. Elongation when testing samples for base metal, laser, and TIG welding was 95%, 67%, and 48%, respectively. The fracture of samples after laser welding during cyclic tests occurred along the base metal, and after TIG welding, fractures occur in red along the weld metal.

Kalacska et al. [123] analyzed the properties of dissimilar joints made of TRIP 800 and TWIP 1000 steels after MIG welding with AWS 307 filler wire. On the TRIP 800 side, the hardness in HAZ increased from 250 HV to 500 HV. On the TWIP 1000 side, the hardness in HAZ decreased from 250 HV to 220 HV. Weldability analysis confirms the serious problem of hardening and softening in the weld and in HAZ when welding the second-generation AHSS, as shown in Figure 13.

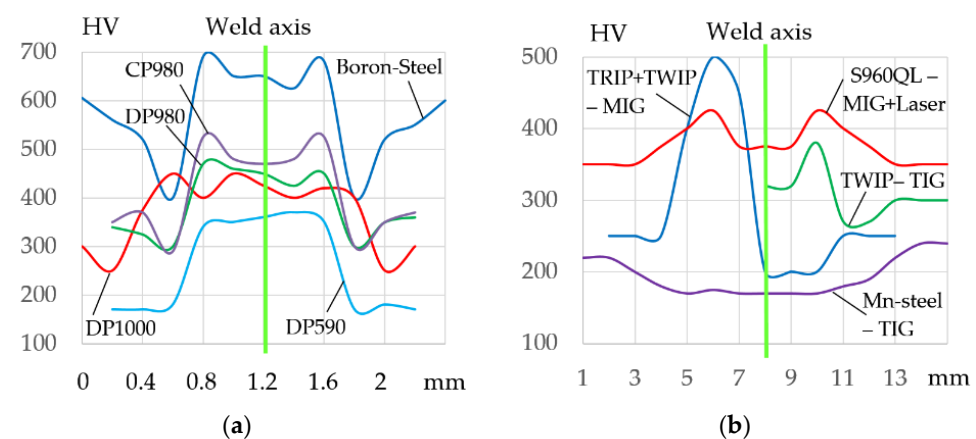


**Figure 13.** Hardness distribution in the cross-section of the joints of AHSS: (a) Laser welding; (b) hybrid and arc welding. Data from [104,105,108,112,115,120–123].

Excellent mechanical properties are achieved during hybrid laser-MAG welding of AHSS as well as when welding dissimilar joints of AHSS with AISI 316 steel [124]. Similar problems with softening in HAZ occur when welding third-generation steels [125]. Laser, resistance welding, and friction-stir welding are used to weld Mn-TRIP steels [126–128]. To develop welding technologies for AHSS, the finite element method is used, which allows predicting the fusion zone, HAZ, the distribution of temperature fields, and mechanical stresses and strains during the welding thermal cycle.

## 7. Improvement of Viscoplasticity of Welded Joints

Welded structures are operated at low temperatures often in hydrogen-containing and corrosive environments. Weldability of steels is complicated by grain growth, hydrogen embrittlement, occurrence of HAC, and decreased impact toughness at low temperatures [129]. The main methods of welding high-strength steels are MIG and MAG welding with solid wire. These methods ensure a minimum content of diffusible hydrogen in the weld metal [130]. Application of hybrid laser-arc welding of HSLA steels with a thickness of over 40 mm also allows obtaining high impact toughness at a temperature of minus 50 °C [131]. A hybrid laser-arc welding of HT780 steel with MGS-80 wire allowed the achievement of the impact energy of 100–150 J at minus 40 °C [132]. Hybrid laser and plasma welding increases the productivity, weld quality, and corrosion resistance of duplex steel welds [133]. A heat treatment after laser welding of 0.3 C-1 Cr-1 Si steel [134] and controlling intermetallic formation during laser welding of NiTi/316L improves the viscoplasticity of welded joints [135].

The microstructural state of the weld and HAZ is the most important factor in the mechanism of hydrogen embrittlement, HAC occurrence, and reduction of impact toughness [136]. A fine-grain microstructure in welding is achieved through an optimal thermal cycle of heating and cooling [137], through reduction of impurities and segregation at grain boundaries [138].

Another effective metallurgical solution is microstructure refinement through the mechanism of heterogeneous nucleation of nonmetallic inclusions and acicular ferrite by forming refractory oxides, sulfides, and nitrides in a weld pool [139]. An effective method of microstructure refinement and removal of impurities is the application of welding consumables with rare-earth elements [140].

Refractory REM oxides and sulfides, such as  $\text{REM}_2\text{O}_3$  and  $\text{REM}_2\text{S}_3$ , are nonmetallic inclusions of spherical shapes, similar to titanium oxides TiO,  $\text{TiO}_2$ , and  $\text{Ti}_2\text{O}_3$  [141]. REM oxides and sulfides have high melting temperatures, °C:  $\text{La}_2\text{O}_3$  (2304);  $\text{Y}_2\text{O}_3$  (2439);  $\text{Ce}_2\text{O}_3$  (2250);  $\text{ThO}_2$  (3350);  $\text{La}_2\text{S}_3$  (2110);  $\text{Y}_2\text{S}_3$  (1925);  $\text{Ce}_2\text{S}_3$  (2450);  $\text{Th}_2\text{S}_3$  (2300). Therefore, the formation of these compounds in the weld pool increases the number of crystallization nuclei. This process contributes to the refinement of microstructure as well as to the nucleation of acicular ferrite [142]. Nonmetallic spherical inclusions of TiO,  $\text{TiO}_2$ , and  $\text{Ti}_2\text{O}_3$  are also effective centers of acicular ferrite nucleation [143]. However, REMs are more active in the reactions of desulfurization and deoxidation of the weld pool [144].

REM borides play an important role in the mechanism of hardening and refinement of the microstructure; they contribute to the formation of refractory boron carbides and the nitrides  $\text{B}_4\text{C}$  and BN [145]. The alloying of boron has a positive effect on the properties and microstructure of cold-resistant and cryogenic austenitic steel with a low residual nitrogen content of up to 0.04% and boron of up to 0.004%. This effect is associated with the solubility of boron in  $\gamma$ -Fe and  $\alpha$ -Fe, reduction of impurities of sulfur S and phosphorus P, and the formation of borides  $\text{Me}_2\text{B}$ ,  $\text{Me}_5\text{B}_3$ ,  $\text{Me}_3(\text{C}, \text{B})$ ,  $\text{Me}_{23}(\text{C}, \text{B})_6$ , and  $\text{FeMo}_2\text{B}_4$  [146].

The formation of free fluorine when introducing fluorides of Ca, Mg, K, and Li into welding consumables is of great importance in welding metallurgy. Fluorine reduces the content of diffusible hydrogen in weld metal due to the formation of the HF compound [147]. High effectiveness of fluorine and fluorides in hydrogen removal is due to the reactions of fluorine and fluorides with the H atom,  $\text{H}_2$  molecule, and  $\text{H}_2\text{O}$  water vapor in the liquid slag and in the plasma of the welding arc [148]. The addition of  $\text{LaF}_3$ ,  $\text{LaB}_6$ , and  $\text{SF}_6$  lead to the improvement of the thermophysical properties of plasma and the quality of arc additive manufacturing products, using G3Si1, 316L, AlMg5Mn1Ti, and  $\text{CuCr}_{0.7}$  wires [149]. The addition of activating fluxes of  $\text{Li}_3\text{AlF}_6$ - $\text{TiO}_2$ - $\text{SiO}_2$  and  $\text{CaF}_2$ - $\text{BaF}_2$ - $\text{SrF}_2$  in the laser welding of steel leads to an increase in the penetration depth up to 33–46% and in productivity up to 45% [150].

In steels and welds, there are the harmful oxides, FeO,  $\text{SiO}_2$ , and MnO, the sulfides, FeS and MnS, as well as diffusible elements, S, H, and N, which reduce the impact toughness, plasticity of welds, and increase sensitivity to the formation of HAC. The alloying of REM

and boron reduces the concentration of the detrimental impurities, S, O, and N. As a result of the interaction, nanodispersed refractory REM oxides, sulfides, and boron nitrides BN are formed, which are the nuclei of primary crystallization. The increase in the number of refractory crystallization nuclei leads to the refinement of large crystallites, dendrites, and microstructures of primary austenitic grains. Parshin et al. [151] proposed the models of dendritic crystallization at the boundary of the “weld pool—base metal” transition without limitation of crystallite growth and with limitation of crystallite growth in the formation of additional crystallization nuclei based on REM oxides and sulfides.

A similar mechanism of dendritic crystallization with crystallization nuclei made of oxides and sulfides is considered in works [152–155]. The alloying of boron into the TWIP steel reduced the size of the austenitic grain from 770 to 344  $\mu\text{m}$  in the columnar and equiaxial zones of the primary crystallites [48]. The formation of nonmetallic spherical inclusions reduces the sensitivity of steels to crack initiation and propagation. After primary crystallization of HSLA steels, secondary recrystallization with pearlitic and bainitic transformation occurs. At that, inside the austenitic grains on the surface of refractory nonmetallic inclusions, intragranular acicular ferrite can nucleate, which inhibits the cracks propagation and increases its trajectory. Parshin et al. [151] proposed the models of crack propagation trajectory in the prior-austenitic grain without acicular ferrite and with acicular ferrite nucleated on a spherical nonmetallic inclusion.

Thus, oxides and sulfides of rare-earth metals and boron nitride contribute to the refinement of primary austenitic microstructures and the nucleation of acicular ferrite in high-strength steels [156–158]. Increasing the volume of acicular ferrite and refinement of weld microstructure is a requirement for increasing impact toughness, reducing the critical temperature of ductile-brittle transition, and reducing sensitivity to the occurrence of HAC. Similar solutions are relevant for underwater wet welding of high-strength steels, as offshore welded structures and pipelines are often located in the Arctic Ocean [146,159,160].

## 8. Conclusions

1. The analysis of research in the field of metallurgy and weldability shows the significant potential of advanced steels for low temperature and cryogenic application. For cold-resistant welded structures HSLA, bainitic, duplex, 1.5–5% Ni steels, and all AHSS steels are recommended. For cryogenic welded structures austenitic Cr-Ni-N-, Mn-, 9% Ni-, Mn-TRIP, and TWIP steels are recommended. For the high quality of welded structures it is necessary to improve weldability and reduce the sensitivity of HSS and AHSS steels of the welding thermal cycle to low temperature and hydrogen embrittlement. The future of the welding of cold-resistant and cryogenic steels lies in microstructure control, reducing the anisotropy of the welded joint-based low heat input in the arc, laser, and hybrid welding with filler REM-containing wires.

2. As for the evolution of TMCP, metallurgy, and welding of high-strength steels, it is necessary for the application of physical and thermodynamic modeling to achieve synergistic effects in the microstructural design. For the manufacturing of isotropic rolled steel, it is necessary to achieve the synergistic effect of the first level considering the microstructure, TMCP parameters, and physical and mechanical properties. For the manufacturing of welded structures, it is necessary to achieve the synergistic effect of the second level considering the structural design, welding metallurgy, microstructure, and welding thermal cycle.

3. Metallurgical processing of high-strength steels for welded structures for cold-resistant and cryogenic service should be based on a special microstructural design. Metallurgy and microstructural design of steels should take into consideration the influence of welding thermal cycles and stresses and repetitive phase transformations in the weld metal and in the heat-affected zone. The distribution and morphology of microstructural phases and nonmetallic inclusions in the matrix are of key factors to achieve high impact toughness and perfect nanometer isotropy of rolled products. Neural network control of TMCP parameters, melting technologies, refining,  $\text{O}_2$ ,  $\text{H}_2$  removal, micro-alloying, devel-

opment of metallurgical fluxes, and slags with rare-earth elements have great potential in the field of fundamental metallurgy.

4. In the field of material science and metallurgy of welding, the fracture micromechanics, models of diffusible hydrogen embrittlement, crystallization kinetics, phase transformations, mechanisms of hardening, and formation of nonmetallic inclusions have great potential. The development of welding consumables with REM, neural network control of the welding thermal cycle, reduction of the softening of welds, increase of the isotropy of welded joints, and monitoring of stresses are very important. Bionic design, weight reduction, application of self-heating, and self-diagnosing are necessary in the design of welded structures for low temperature and cryogenic service.

**Author Contributions:** Conceptualization, A.I.R.; methodology, A.I.R.; formal analysis, S.G.P.; writing—original draft preparation, S.G.P.; writing—review and editing, S.G.P.; visualization, S.G.P.; supervision, A.I.R.; project administration, A.I.R. All authors have read and agreed to the published version of the manuscript.

**Funding:** This research was supported by the project “Energy-efficient systems based on renewable energy for Arctic conditions” (EFREA), KS1054, South-East Finland-Russia CBC Program 2014–2020.

**Institutional Review Board Statement:** Not applicable.

**Informed Consent Statement:** Not applicable.

**Data Availability Statement:** Data sharing is not applicable.

**Conflicts of Interest:** The authors declare no conflict of interest.

## References

1. Rudskoi, A.I. *Scientific Basics in the Control of the Structure and Properties of Steels in the Processes of Thermomechanical Treatment*; Peter the Great St. Petersburg Polytechnic University: Moscow, Russia, 2019.
2. Shigeru, E.; Naoki, N. Development of thermo-mechanical control process (TMCP) and high performance steel in JFE Steel. *JFE Tech. Rep.* **2015**, *20*, 1–7.
3. Buchmayr, B. Thermomechanical Treatment of Steels—A Real Disruptive Technology Since Decades. *Steel Res. Int.* **2017**, *88*, 1700182. [[CrossRef](#)]
4. Bhadeshia, H.K.D.H. *Bainite in Steels. Theory and Practice*, 3rd ed.; CRC Press: Boca Raton, FL, USA, 2018; pp. 367–494.
5. Kalhor, A.; Soleimani, M.; Mirzadeh, H.; Uthaisangsuk, V. A review of recent progress in mechanical and corrosion properties of dual phase steels. *Arch. Civ. Mech. Eng.* **2020**, *20*, 85. [[CrossRef](#)]
6. Nanda, T.; Singh, V.; Singh, V.; Chakraborty, A.; Sharma, S. Third generation of advanced high-strength steels: Processing routes and properties. *Proc. Inst. Mech. Eng. Part L J. Mater. Des. Appl.* **2016**, *233*, 209–238. [[CrossRef](#)]
7. Groth, H.L.; Pillhagen, J.; Vishnu, R.; Jonsson, J.Y. Use of duplex stainless steels at low temperatures. A new way to present toughness-temperature-thickness data. In Proceedings of the Fifth International Experts Seminar on Stainless Steel in Structures, London, UK, 18–19 September 2017; pp. 1–8.
8. Davis, J.R. *Alloying: Understanding the Basics*; ASM International: Materials Park, OH, USA, 2001.
9. Cochrane, R. Phase transformations in microalloyed high strength low alloy (HSLA) steels. In *Phase Transformations in Steels. Diffusionless Transformations, High Strength Steels, Modelling and Advanced Analytical Techniques*, 1st ed.; Woodhead Publishing: Oxford, UK, 2012; pp. 153–212.
10. Shi, L.; Yan, Z.-S.; Liu, Y.-C.; Yang, X.; Zhang, C.; Li, H.-J. Effect of acicular ferrite on banded structures in low-carbon microalloyed steel. *Int. J. Miner. Met. Mater.* **2014**, *21*, 1167–1174. [[CrossRef](#)]
11. Hwang, B.; Gil Lee, C.; Kim, S.-J. Low-Temperature Toughening Mechanism in Thermomechanically Processed High-Strength Low-Alloy Steels. *Met. Mater. Trans. A* **2011**, *42*, 717–728. [[CrossRef](#)]
12. Zhou, X.; Yin, X.; Fang, F.; Jiang, J.; Zhu, W. Influence of rare earths on eutectic carbides in AISI M2 high speed steel. *J. Rare Earths* **2012**, *30*, 1075–1078. [[CrossRef](#)]
13. Ray, A. Niobium microalloying in rail steels. *Mater. Sci. Technol.* **2017**, *33*, 1584–1600. [[CrossRef](#)]
14. Moon, A.; Sangal, S.; Layek, S.; Giribaskar, S.; Mondal, K. Corrosion Behavior of High-Strength Bainitic Rail Steels. *Met. Mater. Trans. A* **2015**, *46*, 1500–1518. [[CrossRef](#)]
15. Pacyna, J. The microstructure and properties of the new bainitic rail steels. *J. Achiev. Mater. Manuf. Eng.* **2008**, *28*, 19–22.
16. Lewis, R.; Olofsson, U. *Wheel-Rail Interface Handbook*, 1st ed.; Woodhead Publishing Limited: Cambridge, UK, 2009.
17. Hajizad, O.; Kumar, A.; Li, Z.; Petrov, R.H.; Sietsma, J.; Dollevoet, R. Influence of Microstructure on Mechanical Properties of Bainitic Steels in Railway Applications. *Metals* **2019**, *9*, 778. [[CrossRef](#)]

18. Liu, Y.; Chen, H.; Liu, Y.; Hang, Z. Simulated HAZ continuous cooling transformation diagram of a bogie steel of high-speed railway. *Int. J. Mod. Phys. B* **2017**, *31*, 1744038. [[CrossRef](#)]
19. Gunn, R.N. *Duplex Stainless Steels. Microstructure, Properties and Applications*; Woodhead Publishing Ltd.: Cambridge, UK, 2003.
20. Calliari, I.; Breda, M.; Gennari, C.; Pezzato, L.; Pellizzari, M.; Zambon, A. Investigation on Solid-State Phase Transformations in a 2510 Duplex Stainless Steel Grade. *Metals* **2020**, *10*, 967. [[CrossRef](#)]
21. Sieurin, H. Fracture Toughness Properties of Duplex Stainless Steels. Ph.D. Thesis, Royal Institute of Technology, Stockholm, Sweden, 2006.
22. Stergiou, V.; Papadimitriou, G.D. Effect of an electron beam surface treatment on the microstructure and mechanical properties of SAF 2205 joints produced with electron beam welding. *J. Mater. Sci.* **2012**, *47*, 2110–2121. [[CrossRef](#)]
23. Wang, H.; Meng, L.; Luo, Q.; Sun, C.; Li, G.; Wan, X. Superior cryogenic toughness of high-Mn austenitic steel by welding thermal cycles: The role of grain boundary evolution. *Mater. Sci. Eng. A* **2020**, *788*, 139573. [[CrossRef](#)]
24. Li, C.; Li, K.; Dong, J.; Wang, J.; Shao, Z. Mechanical behaviour and microstructure of Fe-20/27Mn-4Al-0.3C low magnetic steel at room and cryogenic temperatures. *Mater. Sci. Eng. A* **2021**, *809*, 140998. [[CrossRef](#)]
25. Ren, J.-K.; Chen, Q.-Y.; Chen, J.; Liu, Z.-Y. Role of vanadium additions on tensile and cryogenic-temperature Charpy impact properties in hot-rolled high-Mn austenitic steels. *Mater. Sci. Eng. A* **2021**, *811*, 141063. [[CrossRef](#)]
26. Kim, B.; Lee, S.G.; Kim, D.W.; Jo, Y.H.; Bae, J.; Sohn, S.S.; Lee, S. Effects of Ni and Cu addition on cryogenic-temperature tensile and Charpy impact properties in austenitic 22Mn-0.45C-1Al steels. *J. Alloys Compd.* **2020**, *815*, 152407. [[CrossRef](#)]
27. Martin, A.C.; Oliveira, J.P.; Fink, C. Elemental Effects on Weld Cracking Susceptibility in AlxCoCrCuyFeNi High-Entropy Alloy. *Met. Mater. Trans. A* **2019**, *51*, 778–787. [[CrossRef](#)]
28. Oliveira, J.; Shen, J.; Zeng, Z.; Park, J.M.; Choi, Y.T.; Schell, N.; Maawad, E.; Zhou, N.; Kim, H.S. Dissimilar laser welding of a CoCrFeMnNi high entropy alloy to 316 stainless steel. *Scr. Mater.* **2022**, *206*, 114219. [[CrossRef](#)]
29. Ye, Y.; Wang, Q.; Lu, J.; Liu, C.; Yang, Y. High-entropy alloy: Challenges and prospects. *Mater. Today* **2016**, *19*, 349–362. [[CrossRef](#)]
30. Gali, A.; George, E. Tensile properties of high- and medium-entropy alloys. *Intermetallics* **2013**, *39*, 74–78. [[CrossRef](#)]
31. George, E.P.; Raabe, D.; Ritchie, R.O. High-entropy alloys. *Nature Reviews. Materials* **2019**, *4*, 515–534.
32. Lippold, J.C.; Kotecki, D.J. *Welding Metallurgy and Weldability of Stainless Steels*, 1st ed.; Wiley: Hoboken, NJ, USA, 2005.
33. Raabe, D.; Sun, B.; Da Silva, A.K.; Gault, B.; Yen, H.-W.; Sedighiani, K.; Sukumar, P.T.; Filho, I.R.S.; Katnagallu, S.; Jäggle, E.; et al. Current Challenges and Opportunities in Microstructure-Related Properties of Advanced High-Strength Steels. *Met. Mater. Trans. A* **2020**, *51*, 5517–5586. [[CrossRef](#)]
34. Fonstein, N. *Advanced High Strength Sheet Steels*; Springer: Berlin/Heidelberg, Germany, 2015; pp. 193–195.
35. Dai, Z.; Chen, H.; Ding, R.; Lu, Q.; Zhang, C.; Yang, Z.; van der Zwaag, S. Fundamentals and application of solid-state phase transformations for advanced high strength steels containing metastable retained austenite. *Mater. Sci. Eng. R Rep.* **2021**, *143*, 100590. [[CrossRef](#)]
36. Zhao, J.; Jiang, Z. Thermomechanical processing of advanced high strength steels. *Prog. Mater. Sci.* **2018**, *94*, 174–242. [[CrossRef](#)]
37. Demeri, M.Y. *Advanced High-Strength Steels. Science, Technology, and Applications*; ASM International: Materials Park, OH, USA, 2013.
38. Soleimani, M.; Kalthor, A.; Mirzadeh, H. Transformation-induced plasticity (TRIP) in advanced steels: A review. *Mater. Sci. Eng. A* **2020**, *795*, 140023. [[CrossRef](#)]
39. Ehrhardt, B.; Gerber, T.; Schaumann, T.W. Approaches to microstructural design of TRIP and TRIP aided cold rolled high strength steels. In Proceedings of the International Conference on Advanced High Strength Sheet Steels for Automotive Applications, Association for Iron & Steel Technology, Winter Park, CO, USA, 6–9 June 2004; pp. 39–50.
40. Cao, W.; Zhang, M.; Huang, C.; Xiao, S.; Dong, H.; Weng, Y. Ultrahigh Charpy impact toughness (~450J) achieved in high strength ferrite/martensite laminated steels. *Sci. Rep.* **2017**, *7*, 41459. [[CrossRef](#)]
41. Mazaheri, Y.; Kermanpur, A.; Najafizadeh, A.; Saeidi, N. Effects of initial microstructure and thermomechanical processing parameters on microstructures and mechanical properties of ultrafine grained dual phase steels. *Mater. Sci. Eng. A* **2014**, *612*, 54–62. [[CrossRef](#)]
42. Bräutigam-Matus, K.; Altamirano, G.; Salinas, A.; Flores, A.; Goodwin, F. Experimental Determination of Continuous Cooling Transformation (CCT) Diagrams for Dual-Phase Steels from the Intercritical Temperature Range. *Metals* **2018**, *8*, 674. [[CrossRef](#)]
43. Plchler, A.; Tralnt, S.; Hebesberqer, T.; Stiaszny, P.; Werner, E. Processing of thin sheet multiphase steel grades. *Steel Res. Int.* **2007**, *78*, 216–223. [[CrossRef](#)]
44. Wu, D.; Li, Z.; Lü, H.-S. Effect of Controlled Cooling After Hot Rolling on Mechanical Properties of Hot Rolled TRIP Steel. *J. Iron Steel Res. Int.* **2008**, *15*, 65–70. [[CrossRef](#)]
45. Grajcar, A.; Zalecki, W.; Kuziak, R. Designing of cooling conditions for Si-Al microalloyed TRIP steel on the basis of DCCT diagrams. *J. Achiev. Mater. Manuf. Eng.* **2011**, *45*, 115–124.
46. Mesplont, C. Phase Transformations and Microstructure—Mechanical Properties Relations in Complex Phase High Strength Steels. Ph.D. Thesis, Ghent University, Gent, Belgium, 2002.
47. Zhang, S.; Jiang, Z.; Li, H.; Zhang, B.; Fan, S.; Li, Z.; Feng, H.; Zhu, H. Precipitation behavior and phase transformation mechanism of super austenitic stainless steel S32654 during isothermal aging. *Mater. Charact.* **2018**, *137*, 244–255. [[CrossRef](#)]

48. Salas-Reyes, A.E.; Altamirano-Guerrero, G.; Chávez-Alcalá, J.F.; Barba-Pingarrón, A.; Figueroa, I.A.; Bolarín-Miró, A.M.; Jesús, F.S.-D.; Deaquino-Lara, R.; Salinas, A. Influence of Boron Content on the Solidification Structure, Magnetic Properties and Hot Mechanical Behavior in an Advanced As-Cast TWIP Steel. *Metals* **2020**, *10*, 1230. [[CrossRef](#)]
49. Kozłowska, A.; Radwański, K.; Matus, K.; Samek, L.; Grajcar, A. Mechanical stability of retained austenite in aluminum-containing medium-Mn steel deformed at different temperatures. *Arch. Civ. Mech. Eng.* **2021**, *21*, 19. [[CrossRef](#)]
50. Han, J.; da Silva, A.K.; Ponge, D.; Raabe, D.; Lee, S.-M.; Lee, Y.-K.; Hwang, B. The effects of prior austenite grain boundaries and microstructural morphology on the impact toughness of intercritically annealed medium Mn steel. *Acta Mater.* **2017**, *122*, 199–206. [[CrossRef](#)]
51. Chen, J.; Liu, Z.-Y. The combination of strength and cryogenic impact toughness in low carbon 5Mn–5Ni steel. *J. Alloys Compd.* **2020**, *837*, 155484. [[CrossRef](#)]
52. Yi, H.L.; Chen, P.; Hou, Z.; Hong, N.; Cai, H.; Xu, Y.; Wu, D.; Wang, G. A novel design: Partitioning achieved by quenching and tempering (Q–T & P) in an aluminium-added low-density steel. *Scr. Mater.* **2013**, *68*, 370–374. [[CrossRef](#)]
53. Li, Y.; Liu, D.; Zhang, W.; Kang, J.; Chen, D.; Yuan, G.; Wang, G. Quenching above martensite start temperature in quenching and partitioning (Q&P) steel through control of partial phase transformation. *Mater. Lett.* **2018**, *230*, 36–39. [[CrossRef](#)]
54. Tang, Z.; Huang, J.; Lu, X.; Ding, H.; Zhang, D.; Misra, D. Superior Mechanical Properties and Work-Hardening Ability of Ultrafine-Grained Quenched and Partitioned Steels Processed by a Novel Approach Involving Asymmetric Hot Rolling. *Metals* **2018**, *8*, 872. [[CrossRef](#)]
55. Wang, Z.; Huang, M. Improving Hydrogen Embrittlement Resistance of Hot-Stamped 1500 MPa Steel Parts That Have Undergone a Q&P Treatment by the Design of Retained Austenite and Martensite Matrix. *Metals* **2020**, *10*, 1585. [[CrossRef](#)]
56. Khare, S.; Lee, K.; Bhadeshia, H.K.D.H. Carbide-Free Bainite: Compromise between Rate of Transformation and Properties. *Met. Mater. Trans. A* **2010**, *41*, 922–928. [[CrossRef](#)]
57. Caballero, F.G.; Garcia-Mateo, C.; Capdevila, C.; De Andrés, C.G. Advanced Ultrahigh Strength Bainitic Steels. *Mater. Manuf. Process.* **2007**, *22*, 502–506. [[CrossRef](#)]
58. Chen, X.; Wang, F.; Li, C.; Zhang, J. Dynamic continuous cooling transformation, microstructure and mechanical properties of medium-carbon carbide-free bainitic steel. *High Temp. Mater. Process.* **2020**, *39*, 304–316. [[CrossRef](#)]
59. Pous-Romero, H. Quantitative Basis for the Structure and Properties of a Critically Important Pressure Vessel Steel. Ph.D. Thesis, University of Cambridge, Cambridge, UK, 2015.
60. Smallman, R.; Ngan, A. *Modern Physical Metallurgy*, 8th ed.; Butterworth-Heinemann, Elsevier: Oxford, UK, 2014.
61. Hertzberg, R.W.; Vinci, R.P.; Hertzberg, J.L. *Deformation and Fracture Mechanics of Engineering Materials*, 5th ed.; Wiley: Hoboken, NJ, USA, 2013.
62. Fangnon, E.; Yagodzinskyy, Y.; Malicki, E.; Mehtonen, S.; Virolainen, E.; Vilaça, P. Determination of critical hydrogen concentration and its effect on mechanical performance of 2200 mpa and 600 hbw martensitic ultra-high-strength steel. *Metals* **2021**, *11*, 984. [[CrossRef](#)]
63. Malickii, E.; Fangnon, E.; Vilaça, P. Evaluation of steels susceptibility to hydrogen embrittlement: A thermal desorption spectroscopy-based approach coupled with artificial neural network. *Materials* **2020**, *13*, 5500. [[CrossRef](#)] [[PubMed](#)]
64. Makarov, E.L.; Yakushin, B.F. *Theory of Weldability of Steels and Alloys*; Bauman Moscow State Technical University: Moscow, Russia, 2014. (In Russian)
65. Dadfarnia, M.; Nagao, A.; Wang, S.; Martin, M.L.; Somerday, B.P.; Sofronis, P. Recent advances on hydrogen embrittlement of structural materials. *Int. J. Fract.* **2015**, *196*, 223–243. [[CrossRef](#)]
66. Dwivedi, S.K.; Vishwakarma, M. Effect of hydrogen in advanced high strength steel materials. *Int. J. Hydrogen Energy* **2019**, *44*, 28007–28030. [[CrossRef](#)]
67. Takashima, K.; Yoshioka, Y.; Yokoyama, K.; Funakawa, Y. Hydrogen Embrittlement Behavior of Ultra-high Strength Dual Phase Steel Sheet under Sustained Tensile-loading Test. *ISIJ Int.* **2018**, *58*, 173–178. [[CrossRef](#)]
68. Begic Hadipasic, A.; Malina, J.; Malina, M. The influence of microstructure on hydrogen diffusion and embrittlement of multiphase fine-grained steels with increased plasticity and strength. *Chem. Biochem. Eng. Q.* **2011**, *25*, 159–169.
69. Lovicu, G.; Bottazzi, M.; D’Aiuto, F.; de Sanctis, M.; DiMatteo, A.; Santus, C.; Valentini, R. Hydrogen Embrittlement of Automotive Advanced High-Strength Steels. *Met. Mater. Trans. A* **2012**, *43*, 4075–4087. [[CrossRef](#)]
70. Ryu, J.H.; Chun, Y.S.; Lee, C.S.; Bhadeshia, H.; Suh, D.W. Effect of deformation on hydrogen trapping and effusion in TRIP-assisted steel. *Acta Mater.* **2012**, *60*, 4085–4092. [[CrossRef](#)]
71. Koyama, M.; Akiyama, E.; Tsuzaki, K. Effect of hydrogen content on the embrittlement in a Fe–Mn–C twinning induced plasticity steel. *Corros. Sci.* **2012**, *59*, 277–281. [[CrossRef](#)]
72. Woods, S.; Lee, J.A. *Hydrogen Embrittlement. Technical Memorandum NASA/TM-2016-218602*; NASA Marshall Space Flight Center: Huntsville, AL, USA, 2016; pp. 1–62.
73. Louthan, M.R. Hydrogen Embrittlement of Metals: A Primer for the Failure Analyst. *J. Fail. Anal. Prev.* **2008**, *8*, 289–307. [[CrossRef](#)]
74. Lynch, S.P. Progress towards understanding mechanisms of hydrogen embrittlement and stress corrosion cracking. In Proceedings of the Corrosion Conference and Expo, Nashville, TN, USA, 11–15 March 2007; pp. 1694–1748.
75. Troiano, A.R. The Role of Hydrogen and Other Interstitials in the Mechanical Behavior of Metals. *Met. Microstruct. Anal.* **2016**, *5*, 557–569. [[CrossRef](#)]

76. Oriani, R.A.; Josephic, P.H. Equilibrium aspects of hydrogen-induced cracking of steel. *Acta Metall.* **1974**, *22*, 1065–1074. [[CrossRef](#)]
77. Birnbaum, H.; Sofronis, P. Hydrogen-enhanced localized plasticity—A mechanism for hydrogen-related fracture. *Mater. Sci. Eng. A* **1994**, *176*, 191–202. [[CrossRef](#)]
78. Parshin, S.G. *Metallurgy of Welding*; Politech-Press: Saint-Petersburg, Russia, 2020; pp. 425–436. (In Russian)
79. Sofronis, P.; Birnbaum, H.K. Hydrogen induced shear localization of the plastic flow in metals and alloys. *Eur. J. Mech.-A/Solids* **2001**, *20*, 857–872. [[CrossRef](#)]
80. Sofronis, P.; Birnbaum, H.K. Mechanics of the hydrogen dislocation impurity interactions—I. Increasing shear modulus. *J. Mech. Phys. Solids* **1995**, *43*, 49–90. [[CrossRef](#)]
81. Lynch, S.P. Mechanistic and fractographic aspects of stress-corrosion cracking (SCC). In *Stress Corrosion Cracking: Theory and Practice*; Raja, V.S., Shoji, T., Eds.; Woodhead Publishing: Oxford, UK, 2011; Chapter 1; pp. 3–89.
82. Porubov, A.V.; Belyaev, A.K.; Polyanskiy, V.A. Nonlinear hybrid continuum–discrete dynamic model of influence of hydrogen concentration on strength of materials. *Contin. Mech. Thermodyn.* **2021**, *33*, 933–941. [[CrossRef](#)]
83. Polyanskiy, V.; Belyaev, A.; Chevrychikina, A.; Varshavchik, E.; Yakovlev, Y. Impact of skin effect of hydrogen charging on the Choo-Lee plot for cylindrical samples. *Int. J. Hydrogen Energy* **2021**, *46*, 6979–6991. [[CrossRef](#)]
84. Baykov, A.A. Introduction to metallography of iron, steel and cast iron. *Bull. St. Petersburg Polytech. Inst.* **1911**, *XY*, 527–558. (In Russian)
85. Samarin, A.M. *Physicochemical Bases of Steel Deoxidation*; USSR Academy of Sciences: Moscow, Russia, 1956. (In Russian)
86. Gorynin, V.I.; Olenin, M.I. *Ways to Improve the Cold Resistance of Steel and Welded Joints*; CRISM Prometey: St. Petersburg, Russia, 2017. (In Russian)
87. Lyakishev, N.P.; Pliner, Y.L.; Lappo, S.I. *Boron-Containing Steels and Alloys*; Metallurgy: Moscow, Russia, 1986. (In Russian)
88. Gu, C.; Lian, J.; Bao, Y.; Xiao, W.; Münstermann, S. Numerical Study of the Effect of Inclusions on the Residual Stress Distribution in High-Strength Martensitic Steels During Cooling. *Appl. Sci.* **2019**, *9*, 455. [[CrossRef](#)]
89. Honma, Y.; Sasaki, G.; Hashi, K. Effect of Intercritical Quenching Temperature of Cu-Containing Low Alloy Steel of Long Part Forging for Offshore Applications. *Appl. Sci.* **2019**, *9*, 1705. [[CrossRef](#)]
90. Jiao, Z.B.; Luan, J.; Miller, M.; Chung, Y.; Liu, C. Co-precipitation of nanoscale particles in steels with ultra-high strength for a new era. *Mater. Today* **2017**, *20*, 142–154. [[CrossRef](#)]
91. Samei, J.; Pelligra, C.; Amirmaleki, M.; Wilkinson, D.S. Microstructural design for damage tolerance in high strength steels. *Mater. Lett.* **2020**, *269*, 127664. [[CrossRef](#)]
92. Aoued, S.; Danoix, F.; Allain, S.Y.; Gaudes, S.; Geandier, G.; Hell, J.-C.; Soler, M.; Gouné, M. Microstructure Evolution and Competitive Reactions during Quenching and Partitioning of a Model Fe–C–Mn–Si Alloy. *Metals* **2020**, *10*, 137. [[CrossRef](#)]
93. Ali, M.; Nyo, T.; Kaijalainen, A.; Hannula, J.; Porter, D.; Kömi, J. Influence of Chromium Content on the Microstructure and Mechanical Properties of Thermomechanically Hot-Rolled Low-Carbon Bainitic Steels Containing Niobium. *Appl. Sci.* **2020**, *10*, 344. [[CrossRef](#)]
94. Kvackaj, T.; Bidulská, J.; Bidulský, R. Overview of HSS steel grades development and study of reheating condition effects on austenite grain size changes. *Materials* **2021**, *14*, 1988. [[CrossRef](#)]
95. Kostryzhev, A.; Marenych, O. New Technology to Produce 1 GPa Low Carbon Microalloyed Steels from Cast Strip. *Metals* **2018**, *8*, 662. [[CrossRef](#)]
96. Shen, Y.; Jia, N.; Wang, Y.; Sun, X.; Zuo, L.; Raabe, D. Suppression of twinning and phase transformation in an ultrafine grained 2 GPa strong metastable austenitic steel: Experiment and simulation. *Acta Mater.* **2015**, *97*, 305–315. [[CrossRef](#)]
97. Forouzan, F.; Najafzadeh, A.; Kermanpur, A.; Hedayati, A.; Surkialabad, R. Production of nano/submicron grained AISI 304L stainless steel through the martensite reversion process. *Mater. Sci. Eng. A* **2010**, *527*, 7334–7339. [[CrossRef](#)]
98. Järvenpää, A.; Jaskari, M.; Kisko, A.; Karjalainen, P. Processing and Properties of Reversion-Treated Austenitic Stainless Steels. *Metals* **2020**, *10*, 281. [[CrossRef](#)]
99. Wang, C.; Lin, X.; Wang, L.; Zhang, S.; Huang, W. Cryogenic mechanical properties of 316L stainless steel fabricated by selective laser melting. *Mater. Sci. Eng. A* **2021**, *815*, 141317. [[CrossRef](#)]
100. Xiong, Z.; Timokhina, I.; Pereloma, E. Clustering, nano-scale precipitation and strengthening of steels. *Prog. Mater. Sci.* **2021**, *118*, 100764. [[CrossRef](#)]
101. Lesch, C.; Kwiaton, N.; Klose, F.B. Advanced High Strength Steels (AHSS) for Automotive Applications—Tailored Properties by Smart Microstructural Adjustments. *Steel Res. Int.* **2017**, *88*, 1–22. [[CrossRef](#)]
102. Bhadeshia, H.K.D.H. Neural Networks in Materials Science. *ISIJ Int.* **1999**, *39*, 966–979. [[CrossRef](#)]
103. Solano-Alvarez, W.; Peet, M.; Pickering, E.; Jaiswal, J.; Bevan, A.; Bhadeshia, H. Synchrotron and neural network analysis of the influence of composition and heat treatment on the rolling contact fatigue of hypereutectoid pearlitic steels. *Mater. Sci. Eng. A* **2017**, *707*, 259–269. [[CrossRef](#)]
104. Kim, K.; Kang, N.; Kang, M.; Kim, C. Assessment of Heat-Affected Zone Softening of Hot-Press-Formed Steel over 2.0 GPa Tensile Strength with Bead-On-Plate Laser Welding. *Appl. Sci.* **2021**, *11*, 5774. [[CrossRef](#)]
105. Urbańczyk, M.; Banasik, M.; Stano, S.; Adamiec, J. Effect of Hybrid Laser Arc Welding on the Structure and Properties of High Yield Point Steel S960QL. *Biul. Inst. Spaw.* **2018**, *2018*, 183–190. [[CrossRef](#)]
106. Kang, H.T.; Khosrovaneh, A.; Link, T.; Bonnen, J.; Amaya, M.; Shih, H.-C. The Effect of Welding Dimensional Variability on the Fatigue Life of Gas Metal Arc Welded Joints. *SAE Int. J. Mater. Manuf.* **2011**, *4*, 298–313. [[CrossRef](#)]

107. Mostaan, H.; Saeedpour, P.; Ahmadi, H.; Nouri, A. Laser welding of dual-phase steels with different silicon contents: Phase evolutions, microstructural observations, mechanical properties, and fracture behavior. *Mater. Sci. Eng. A* **2021**, *811*, 140974. [[CrossRef](#)]
108. Alves, P.; Lima, M.; Raabe, D.; Sandim, H. Laser beam welding of dual-phase DP1000 steel. *J. Mater. Process. Technol.* **2018**, *252*, 498–510. [[CrossRef](#)]
109. Xue, X.; Pereira, A.B.; Amorim, J.; Liao, J. Effects of Pulsed Nd:YAG Laser Welding Parameters on Penetration and Microstructure Characterization of a DP1000 Steel Butt Joint. *Metals* **2017**, *7*, 292. [[CrossRef](#)]
110. He, H.; Forouzan, F.; Volpp, J.; Robertson, S.; Vuorinen, E. Microstructure and Mechanical Properties of Laser-Welded DP Steels Used in the Automotive Industry. *Materials* **2021**, *14*, 456. [[CrossRef](#)]
111. Farabi, N.; Chen, D.; Zhou, Y. Fatigue properties of laser welded dual-phase steel joints. *Procedia Eng.* **2010**, *2*, 835–843. [[CrossRef](#)]
112. Sun, Q.; Di, H.-S.; Li, J.; Wang, X.-N. Effect of pulse frequency on microstructure and properties of welded joints for dual phase steel by pulsed laser welding. *Mater. Des.* **2016**, *105*, 201–211. [[CrossRef](#)]
113. Morawiec, M.; Grajcar, A. Metallurgical aspects of weldability of multiphase steels for automotive industry. *Appl. Eng. Lett.* **2017**, *2*, 38–42.
114. Rozanski, M.; Morawiec, M.; Grajcar, A.; Stano, S. Modified Twin-Spot Laser Welding of Complex Phase Steel. *Arch. Met. Mater.* **2016**, *61*, 1999–2008. [[CrossRef](#)]
115. Martin-Root, C.K.H. Laser Welding of Complex Phase and Dual Phase Advanced High Strength Steels—The Effects That Welding Has on Microstructure and Formability. Ph.D. Thesis, University of Waterloo, Waterloo, ON, Canada, 2020.
116. Roncery, L.M.; Weber, S.; Theisen, W. Welding of twinning-induced plasticity steels. *Scr. Mater.* **2012**, *66*, 997–1001. [[CrossRef](#)]
117. Saha, D.C.; Cho, Y.; Park, Y.-D. Metallographic and fracture characteristics of resistance spot welded TWIP steels. *Sci. Technol. Weld. Join.* **2013**, *18*, 711–720. [[CrossRef](#)]
118. Han, I.-W.; Eom, J.-B.; Yun, J.-G.; Lee, B.-G.; Kang, C.-Y. Microstructure and Hardness of 1st layer with Crystallographic Orientation of Solidification Structure in Multipass Weld using High Mn-Ni Flux Cored Wire. *J. Weld. Join.* **2016**, *34*, 77–82. [[CrossRef](#)]
119. Park, G.; Kim, B.; Kang, Y.; Kang, H.; Lee, C. Characterization of bond line discontinuities in a high-Mn TWIP steel pipe welded by HF-ERW. *Mater. Charact.* **2016**, *118*, 14–21. [[CrossRef](#)]
120. Park, G.-W.; Jo, H.; Park, M.; Shin, S.; Ko, W.-S.; Park, N.; Kim, B.-J.; Ahn, Y.-S.; Jeon, J.B. Microstructure and Mechanical Properties of Gas Tungsten Arc Welded High Manganese Steel Sheet. *Metals* **2019**, *9*, 1167. [[CrossRef](#)]
121. Podany, P.; Reardon, C.; Koukolikova, M.; Prochazka, R.; Franc, A. Microstructure, Mechanical Properties and Welding of Low Carbon, Medium Manganese TWIP/TRIP Steel. *Metals* **2018**, *8*, 263. [[CrossRef](#)]
122. Ma, L.-L.; Wei, Y.-H.; Hou, L.-F.; Yan, B. Microstructure and Mechanical Properties of TWIP Steel Joints. *J. Iron Steel Res. Int.* **2014**, *21*, 749–756. [[CrossRef](#)]
123. Kalácska, E.; Májlínger, K.; Fábíán, E.R.; Spena, P.R. MIG-Welding of Dissimilar Advanced High Strength Steel Sheets. *Mater. Sci. Forum* **2017**, *885*, 80–85. [[CrossRef](#)]
124. Perulli, P.; Dassisti, M.; Casalino, G. Thermo-Mechanical Simulation of Hybrid Welding of DP/AISI 316 and TWIP/AISI 316 Dissimilar Weld. *Materials* **2020**, *13*, 2088. [[CrossRef](#)]
125. Pereira, A.B.; Santos, R.O.; Carvalho, B.S.; Butuc, M.C.; Vincze, G.; Moreira, L.P. The Evaluation of Laser Weldability of the Third-Generation Advanced High Strength Steel. *Metals* **2019**, *9*, 1051. [[CrossRef](#)]
126. Kang, M.; Kim, Y.-M.; Han, H.N.; Kim, C. Effects of Phase Evolution on Mechanical Properties of Laser-Welded Ferritic Fe-Al-Mn-C Steel. *Metals* **2017**, *7*, 523. [[CrossRef](#)]
127. Stadler, M.; Schnitzer, R.; Gruber, M.; Steineder, K.; Hofer, C. Microstructure and Local Mechanical Properties of the Heat-Affected Zone of a Resistance Spot Welded Medium-Mn Steel. *Materials* **2021**, *14*, 3362. [[CrossRef](#)]
128. Mironov, S.; Sato, Y.; Yoneyama, S.; Kokawa, H.; Fujii, H.; Hirano, S. Microstructure and tensile behavior of friction-stir welded TRIP steel. *Mater. Sci. Eng. A* **2018**, *717*, 26–33. [[CrossRef](#)]
129. Villalobos, J.C.; Del-Pozo, A.; Campillo, B.; Mayén, J.; Serna, S. Microalloyed Steels through History until 2018: Review of Chemical Composition, Processing and Hydrogen Service. *Metals* **2018**, *8*, 351. [[CrossRef](#)]
130. Viyanit, E.; Keawkumsai, S.; Wongpinkeaw, K.; Bunchoo, N.; Khonraeng, W.; Trachoo, T.; Boellinghaus, T. Hydrogen assisted cracking of an AISI 321 stainless steel seamless pipe exposed to hydrogen-containing hot gas at high pressure. *Eng. Fail. Anal.* **2019**, *100*, 288–299. [[CrossRef](#)]
131. Bunaziv, I.; Akselsen, O.M.; Frostevarg, J.; Kaplan, A.F.H. Application of laser-arc hybrid welding of steel for low-temperature service. *Int. J. Adv. Manuf. Technol.* **2019**, *102*, 2601–2613. [[CrossRef](#)]
132. Pan, Q.; Mizutani, M.; Kawahito, Y.; Katayama, S. Effect of shielding gas on laser-MAG arc hybrid welding results of thick high-tensile-strength steel plates. *Weld. World* **2016**, *60*, 653–664. [[CrossRef](#)]
133. Verma, J.; Taiwade, R.V. Effect of welding processes and conditions on the microstructure, mechanical properties and corrosion resistance of duplex stainless steel weldments—A review. *J. Manuf. Process.* **2017**, *25*, 134–152. [[CrossRef](#)]
134. Kuryntsev, S.V.; Gilmudtinov, A.K. Heat treatment of welded joints of steel 0.3C–1Cr–1Si produced by high-power fiber lasers. *Opt. Laser Technol.* **2015**, *74*, 125–131. [[CrossRef](#)]
135. Shamsolhodaei, A.; Oliveira, J.; Schell, N.; Maawad, E.; Panton, B.; Zhou, Y. Controlling intermetallic compounds formation during laser welding of NiTi to 316L stainless steel. *Intermetallics* **2020**, *116*, 106656. [[CrossRef](#)]

136. Artola, G.; Arredondo, A.; Fernández-Calvo, A.I.; Aldazabal, J. Hydrogen Embrittlement Susceptibility of R4 and R5 High-Strength Mooring Steels in Cold and Warm Seawater. *Metals* **2018**, *8*, 700. [[CrossRef](#)]
137. Królicka, A.; Ambroziak, A.; Żak, A. Welding Capabilities of Nanostructured Carbide-Free Bainite: Review of Welding Methods, Materials, Problems, and Perspectives. *Appl. Sci.* **2019**, *9*, 3798. [[CrossRef](#)]
138. Nunes, A.R.V.; Zeemann, A.; de Almeida, L.H. The contribution of impurities to unexpected cold cracks in a thick C-Mn steel plate. *J. Mater. Res. Technol.* **2019**, *8*, 4364–4373. [[CrossRef](#)]
139. Yi, H.-J.; Lee, Y.-J.; Kim, J.-Y.; Kang, S.-S. Effect of microstructure and chemical composition on cold crack susceptibility of high-strength weld metal. *J. Mech. Sci. Technol.* **2011**, *25*, 2185–2193. [[CrossRef](#)]
140. Parshin, S.G. Metallurgical Effect of Rare-Earth Lanthanum Fluoride and Boride in the Composite Coating of Wires in the Arc Welding of Bainitic-Martensitic and Austenitic Steel. *Metals* **2020**, *10*, 1334. [[CrossRef](#)]
141. Shang, Z.; Li, T.; Yang, S.; Yan, J.; Guo, H. Three-dimensional characterization of typical inclusions in steel by X-ray Micro-CT. *J. Mater. Res. Technol.* **2020**, *9*, 3686–3698. [[CrossRef](#)]
142. Adabavazeh, Z.; Hwang, W.S.; Su, Y.H. Effect of Adding Cerium on Microstructure and Morphology of Ce-Based Inclusions Formed in Low-Carbon Steel. *Sci. Rep.* **2017**, *7*, 46503. [[CrossRef](#)] [[PubMed](#)]
143. Milani, J.M.; Saeid, T. Acicular ferrite nucleation and growth in API5L-X65 steel submerged arc welded joints. *Mater. Sci. Technol.* **2020**, *36*, 1398–1406. [[CrossRef](#)]
144. Luo, S.; Shen, Z.; Yu, Z.; Wang, W.; Zhu, M. Effect of Ce Addition on Inclusions and Grain Structure in Gear Steel 20CrNiMo. *Steel Res. Int.* **2021**, *92*, 1–20. [[CrossRef](#)]
145. Wang, Y.; Yan, Q. Microstructure and strengthening mechanism of grain boundary strengthened W-ZrB<sub>2</sub> alloy. *J. Mater. Res. Technol.* **2020**, *9*, 4007–4015. [[CrossRef](#)]
146. Bai, J.; Cui, Y.; Wang, J.; Dong, N.; Qurashi, M.S.; Wei, H.; Yang, Y.; Han, P. Effect of Boron Addition on the Precipitation Behavior of S31254. *Metals* **2018**, *8*, 497. [[CrossRef](#)]
147. Parshin, S.G.; Levchenko, A.M.; Maystro, A.S. Metallurgical Model of Diffusible Hydrogen and Non-Metallic Slag Inclusions in Underwater Wet Welding of High-Strength Steel. *Metals* **2020**, *10*, 1498. [[CrossRef](#)]
148. Parshin, S.G.; Levchenko, A.M.; Karkhin, V.A.; Wang, P.; Maystro, A.S. Metallurgy of electrochemical ionic processes in molten slag during underwater wet arc welding. In Proceedings of the 31st (2021) International Ocean and Polar Engineering Conference, Rhodes, Greece, 20–25 June 2021; pp. 1–5.
149. Parshin, S.G.; Mayr, P. Thermophysical Properties of Electric Arc Plasma and the Wire Melting Effect with Lanthanum and Sulfur Fluorides Addition in Wire Arc Additive Manufacturing. *Metals* **2021**, *11*, 1756. [[CrossRef](#)]
150. Parshin, S.G.; Parshin, S.S.; Burkner, G.; Semmler, W.; Kusch, M.; Henig, T.; Khun, S. Effect of ultrafine particles of activating fluxes on the laser welding process. *Weld. Int.* **2011**, *25*, 545–549. [[CrossRef](#)]
151. Parshin, S.; Karkhin, V.; Mayr, P.; Maystro, A. The Effect of Electrochemical Composite Coatings with LaF<sub>3</sub>-LaB<sub>6</sub> Particles in Nickel-Copper Matrix on the Metallurgical Processes in Arc Welding of Low Alloy Ferrite-Pearlite Steels. *Materials* **2021**, *14*, 1509. [[CrossRef](#)]
152. Boniardi, M.; Casaroli, A. *Steel Metallurgy*; Politecnico: Milan, Italy, 2017; Volume I, p. 51.
153. Campbell, J. *Castings*; Butterworth-Heinemann: Oxford, UK, 2017; p. 135.
154. You, D.; Michelic, S.K.; Presoly, P.; Liu, J.; Bernhard, C. Modeling inclusion formation during solidification of steel: A review. *Metals* **2017**, *7*, 460. [[CrossRef](#)]
155. Terazawa, Y.; Ichimiya, K.; Hase, K. Nucleation Effect of Ca-Oxysulfide Inclusions of Low Carbon Steel in Heat Affected Zone by Welding. *Mater. Sci. Forum* **2018**, *941*, 130–134. [[CrossRef](#)]
156. Li, Y.-W.; Liu, H.-T.; Wang, Z.-J.; Zhang, Z.-H.; Li, W.-T.; Shen, H.-Y.; Zhang, X.-M.; Wang, G.-D. Solidification microstructure of high borated stainless steels with rare earth and titanium additions. *Rare Met.* **2019**, *39*, 1483–1491. [[CrossRef](#)]
157. Yamada, T.; Terasaki, H.; Komizo, Y.-I. Relation between Inclusion Surface and Acicular Ferrite in Low Carbon Low Alloy Steel Weld. *ISIJ Int.* **2009**, *49*, 1059–1062. [[CrossRef](#)]
158. Loder, D.; Michelic, S.K.; Bernhard, C. Acicular Ferrite Formation and Its Influencing Factors—A Review. *J. Mater. Sci. Res.* **2016**, *6*, 24. [[CrossRef](#)]
159. Tomków, J.; Fydrych, D.; Rogalski, G. Dissimilar underwater wet welding of HSLA steels. *Int. J. Adv. Manuf. Technol.* **2020**, *109*, 717–725. [[CrossRef](#)]
160. Parshin, S.G.; Levchenko, A.M.; Wang, P. Metallurgy and Mechanism of Underwater Wet Cutting Using Oxidizing and Exothermic Flux-Cored Wires. *Materials* **2021**, *14*, 4655. [[CrossRef](#)] [[PubMed](#)]